J. Fluid Mech. (2012), *vol.* 710, *pp.* 324–361.
doi:10.1017/jfm.2012.366

Shear instability of internal solitary waves in Euler fluids with thin pycnoclines

A. Almgren[1], R. Camassa[2] and R. Tiron[3]†

[1] Lawrence Berkeley National Laboratory, Berkeley, CA 94720, USA

[2] Carolina Center for Interdisciplinary Applied Mathematics, Department of Mathematics, University of North Carolina, Chapel Hill, NC 27599-3250, USA

[3] UCD School of Mathematical Sciences, University College Dublin, Belfield, Dublin 4, Ireland

(Received 14 August 2011; revised 13 April 2012; accepted 17 July 2012; first published online 29 August 2012)

The stability with respect to initial condition perturbations of solitary travelling-wave solutions of the Euler equations for continuously, stably stratified, near two-layer fluids is examined numerically and analytically for a set of parameters of relevance for laboratory experiments. Numerical travelling-wave solutions of the Dubreil–Jacotin–Long equation are first obtained with a variant of Turkington, Eyland and Wang's iterative code by testing convergence on the equation's residual. In this way, stationary solutions with very thin pycnoclines (and small Richardson numbers) approaching the near two-layer configurations used in experiments can be obtained, allowing for a stability study free of non-stationary effects, introduced by lack of numerical resolution, which develop when these solutions are used as initial conditions in a time-dependent evolution code. The thin pycnoclines in this study permit analytical results to be derived from strongly nonlinear models and their predictions compared with carefully controlled numerical simulations. This brings forth shortcomings of simple criteria for shear instability manifestations based on parallel shear approximations due to subtle higher-order effects. In particular, evidence is provided that the fore–aft asymmetric growth observed in all simulations requires non-parallel shear analysis. Collectively, the results of this study reveal that while the wave-induced shear can locally reach unstable configurations and give rise to local convective instability, the global wave/self-generated shear system is in fact stable, even for extreme cases of thin pycnoclines and near-maximum-amplitude waves.

Key words: absolute/convective instability, internal waves, shear layers

1. Introduction

Field as well as laboratory experiments in recent years have revealed that internal wave motion, and in particular its form of near-solitary travelling waves, is ubiquitous in geophysics and can commonly attain large displacements of density isolines from equilibrium (see e.g. the review by Helfrich & Melville 2006), challenging the usefulness of theoretical models based on small amplitude asymptotics. The renewed attention to large-amplitude motion has also illustrated, with both field (Moum *et al.* 2003; Duda *et al.* 2004) and laboratory measurements (Grue *et al.* 1999; Fructus *et al.* 2009), how shear instability in the form of Kelvin–Helmholtz rolls can be

† Email address for correspondence: roxana.tiron@gmail.com

self-induced when wave amplitudes become sufficiently large, and direct numerical simulations have further demonstrated (Tiron 2009; Barad & Fringer 2010) that this instability can be governed by the appropriate Euler (or Navier–Stokes) equations. While all these works have provided ample evidence that self-induced shear from internal wave motion can become unstable, most of these studies have illustrated this in the context of *time-evolving, near-solitary* waves. This of course is unavoidable in field and even in laboratory experiments, where solitary waves can only be created by either natural or manufactured classes of initial/boundary conditions which ensure their structural emergence only over some finite time–space scales. Thus, the evolution towards solitary-wave motion can mask the true dynamics of solitary-wave instability in these studies. Naturally, for experiments, and to an even greater extent for their field counterparts, an unambiguous determination of the onset of instability may be affected by several other unrelated causes.

Renewed attention is being paid to this class of problems from a numerical viewpoint, e.g. Carr, King & Dritschel (2011) and Lamb & Farmer (2011), with a focus on the shear instability of solitary internal wave solutions via direct numerical simulations in the framework of the so-called Boussinesq approximation of neglecting fluid inertia. These studies adopt complementary viewpoints: Carr *et al.* (2011) are concerned with the 'free' travelling-wave problem set-up, whereby the infinite line in the horizontal coordinate is emulated with large periodic domains, while Lamb & Farmer (2011) study the 'forced' problem with inflow–outflow boundary conditions, in the stationary wave frame. All these studies point to the evidence of shear instabilities, when solitary-wave amplitudes become large and/or the pycnocline region of the quiescent stratified fluid becomes sufficiently thin.

Despite the recent attention to this class of problems, it seems that a study that draws a distinction between the instability of the self-induced shear and that of the whole wave solution is still missing. This would imply adopting the viewpoint of stability in the sense of Lyapunov (see e.g. Arnold 1992) of solitary travelling wave solutions of the governing Euler equations. Thus, according to this definition, stability would require finding an appropriate norm to define a perturbation neighbourhood of the travelling-wave solution, and show that initial conditions chosen within this neighbourhood stay for all time close to the travelling wave as measured by a related norm. Reducing the size of the perturbation makes the closeness in this norm approach zero. Unfortunately, compounding the known obstacles to proving stability in this sense for stratified flows (as noticed, among others, by Benjamin 1986 and Friedlander 2001) there remains the fact that travelling-wave solutions, whose perturbed evolution could then be studied analytically or numerically, are not known in closed form. This makes such a stability study difficult, as finding unperturbed solutions also has to rely on numerical tools. Furthermore, as noted by Long (1965) and Benjamin (1966), the Boussinesq approximation can be problematic for (large) internal waves: to avoid its limitations we have to retain the extra physics of the original Euler equations and hence the added mathematical complexity. This situation is somewhat helped by analytical solutions from asymptotic models, which are particularly effective (see e.g. Camassa *et al.* 2006) when the pycnocline is rather thin and sandwiched between two layers of homogeneous density. When the smoothly stratified fluid is close to this limit, closed-form solutions for travelling waves for all amplitudes (up to their degenerate limit to conjugate states) are available in terms of tabulated functions, and can be used to reconstruct the velocity field. This in turn provides asymptotic approximations for the wave-induced shear, making possible some predictions of stability parameters, such as local Richardson number and length scales of the unstable shear regions.

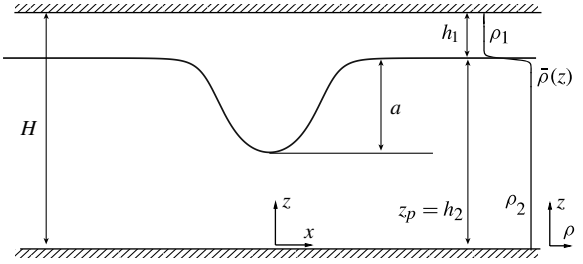

FIGURE 1. The stratified fluid set-up and relevant notation.

The set-up we consider is motivated by the experiments of Grue *et al.* (1999), and we use the dimensional parameters of those experiments throughout this work to anchor our analysis to a physically realizable case. We assume the dynamics is governed by the incompressible stratified Euler equations for a fluid in the two-dimensional strip $-L/2 < x < L/2$, $0 < z < H$, between slip impenetrable walls, with velocity (u, w), pressure p, and density ρ satisfying

$$u_x + w_z = 0, \tag{1.1}$$

$$u_t + uu_x + wu_z = -p_x/\rho, \tag{1.2}$$

$$w_t + uw_x + ww_z = -p_z/\rho - g, \tag{1.3}$$

$$\rho_t + u\rho_x + w\rho_z = 0, \tag{1.4}$$

where $g = 981$ cm s^{-2} is the acceleration of gravity. The lateral boundary conditions for all physical quantities are assumed to decay (sufficiently fast) to equilibrium if $L \to \infty$, or L-periodic for numerical implementations, with L sufficiently large. In order to model the diffused salt interface, we choose for the smooth background density stratification the antisymmetric profile

$$\overline{\rho}(z) = \rho_{min} + \frac{\rho_{max} - \rho_{min}}{2}\left(1 + \tanh\left[\gamma(z_p - z)\right]\right), \quad z \in [0, H], \tag{1.5}$$

where ρ_{min}, ρ_{max} are the densities below and above the pycnocline, z_p is the location of the inflection point (the centre) of the density stratification, and γ is a parameter inversely proportional to the thickness of the pycnocline. We define this thickness as the distance between the points of 10 and 90 % of the total density variation, i.e. the vertical locations in the density stratification corresponding to $\rho_{min} + 0.1\Delta\rho$ and $\rho_{max} - 0.1\Delta\rho$, respectively. We fix the densities $\rho_{min} = 0.999$ g cm^{-3}, $\rho_{max} = 1.022$ g cm^{-3}, the total height of the fluid column $H = 77$ cm, the parameter $\gamma \approx 1.033$ cm^{-1} (corresponding to a relatively thin pycnocline of approximately 2 cm) and the centre of the pycnocline of the undisturbed configuration located at 62 cm. For a definition of wave amplitude, we take the maximum displacement of the average density isoline, and denote by $h_1 = H - z_p$ and $h_2 = z_p$ the widths of upper and lower layer, respectively, for the reference density stratification (1.5). See figure 1 for a sketch of the set-up. While the functional form (1.5) is different from an error function, which can be expected to develop from salt diffusivity between two homogeneous layers, we have verified that most of our results are largely independent of different functional forms of the stratification in the thin pycnocline limit.

Our stability study begins in § 2 with the task of producing accurate travelling internal wave solutions to be used as initial conditions in a time-evolution code. The numerical algorithm of Turkington, Eydeland & Wang (1991) (henceforth referred

to as TEW) is adapted to our purposes for thin pycnoclines. Next, by using the iteration code solutions as initial conditions, in § 3 we carry out a validation study of an incompressible Euler (and Navier–Stokes) variable density solver based on a conservative projection method for the time-dependent flows in two dimensions (VARDEN), described in detail in Almgren *et al.* (1998). Once we are able to discern between numerically induced time-dependence and true shear instability, we study in § 4 the stability of travelling-wave solutions with respect to the initial value perturbation problem. The VARDEN code is used to provide the evolution of initial perturbations for waves with unstable shear tested against the predictions from the spectral analysis of flow linearization around the wave-induced shear background. In particular, we test a simple criterion for predicting the development of shear instability based on the combined approximations of strongly nonlinear long-wave models, envelope equations for disturbance growth and local shear eigenvalue analysis. We provide details of our numerical implementations and tests in the appendices.

2. Convergence of the TEW algorithm for thin pycnoclines

In this section we describe our numerical implementation of the TEW algorithm (Turkington *et al.* 1991). Seeking travelling-wave solutions of the Euler system (1.1)–(1.4) leads to the so-called Dubreil–Jacotin–Long (DJL) equation (see e.g. Yih 1980, p. 104, and Turkington *et al.* 1991)

$$\mathrm{M}\,\eta = \frac{\lambda\eta}{H}\,\overline{\rho}'(z-\eta) \quad \text{in } D, \quad \eta = 0 \quad \text{on } \partial D, \quad \eta \to 0 \quad \text{as } x \to \pm\infty, \tag{2.1}$$

where $D = \{(x,z) \in \mathbb{R}^2 : -\infty < x < \infty, 0 < z < H\}$ denotes the fluid domain, $\overline{\rho}(z)$ is the background stratification, $\overline{\rho}'(z)$ denotes derivative with respect to its argument z, M denotes the quasi-linear elliptical operator

$$\mathrm{M}\,\eta \equiv -(\overline{\rho}(z-\eta)\eta_x)_x - (\overline{\rho}(z-\eta)\eta_z)_z - \tfrac{1}{2}\,|\nabla\eta|^2\,\overline{\rho}'(z-\eta), \tag{2.2}$$

and λ is an eigenvalue-like parameter defined in terms of the wave travelling speed c by

$$\lambda = \frac{gH}{c^2}. \tag{2.3}$$

Assuming that there are no closed isopycnal surfaces, (2.1) determines the unknown function $\eta(x,z)$, which represents the vertical displacement of the isopycnal surface passing through the point (x,z) from its undisturbed level at $\pm\infty$ (in the above we have suppressed the arguments of this displacement function for ease of notation). This form of the DJL equation is further modified by Turkington *et al.* (1991), who exploit an ingenious change of variables and a variational structure for the equation to implement a recurrence algorithm for its solutions. For completeness, we report some details of their method in appendix A, while concentrating here on the main steps. First, by replacing η in favour of a new unknown ϕ,

$$\phi = s(z) - s(z-\eta) \quad \text{with } s(z) = \int_0^z \sqrt{\overline{\rho}(\xi)}\,\mathrm{d}\xi, \tag{2.4}$$

the quasi-linear eigenvalue problem in η (2.1) turns into a semilinear eigenvalue problem in ϕ:

$$-\Delta\phi + e_\phi(z,\phi) - \lambda f_\phi(z,\phi) = 0, \quad \phi = 0 \quad \text{on } \partial D, \quad \phi \to 0 \quad \text{as } x \to \pm\infty \tag{2.5}$$

(see § A.2 for the definitions of the functionals e_ϕ, f_ϕ and for further details on this transformation). This semilinear eigenvalue problem can be solved iteratively thanks to the variational structure (see § A.3 for an outline of the procedure).

The explicit construction of the iterative scheme that determines a solution of the DJL equation for a given stratification $\overline{\rho}(z)$ with a prescribed available potential energy A (defined by (A 2)) is reducible to the following three steps.

(i) Solve the two elliptic boundary value problems (for the two unknowns v^k and w^k)

$$(-\Delta + \alpha)v^k = \alpha\phi^k - e_\phi(z, \phi) \quad \text{in } D, \quad v^k = 0 \quad \text{on } \partial D, \tag{2.6}$$

$$(-\Delta + \alpha)w^k = f_\phi(z, \phi) \quad \text{in } D, \quad w^k = 0 \quad \text{on } \partial D. \tag{2.7}$$

(ii) Evaluate the four integrals

$$S_1 = \int_D f_\phi(z, \phi^k)w^k \,\mathrm{d}x\,\mathrm{d}z, \tag{2.8}$$

$$S_2 = \int_D f_\phi(z, \phi^k)(\phi^k - v^k) \,\mathrm{d}x\,\mathrm{d}z, \tag{2.9}$$

$$S_3 = \int_D \left[|\nabla(\phi^k - v^k)|^2 + \alpha\,(\phi^k - v^k)^2\right] \,\mathrm{d}x\,\mathrm{d}z, \tag{2.10}$$

$$F = \int_D f(z, \phi^k) \,\mathrm{d}x\,\mathrm{d}z. \tag{2.11}$$

(iii) Define the iteration step by relating the auxiliary functions v^k and w^k to the updated DJL unknowns (ϕ, λ)

$$\mu^{k+1} = \max\left[0, \frac{A - F(\phi^k) + S_2 + \beta S_3}{S_1 + 2\beta S_2 + \beta^2 S_3}\right], \tag{2.12}$$

$$\phi^{k+1} = v^k + \mu^{k+1}[w^k + \beta(\phi^k - v^k)], \tag{2.13}$$

$$\lambda^k = \frac{\mu^k}{1 - \beta\mu^k}. \tag{2.14}$$

In the above, α, β are two parameters that control the convexity of the functionals involved in the iterative scheme (see relations (A 15) and (A 17) for their definition).

As observed in Turkington *et al.* (1991), the convergence of the TEW algorithm is greatly reduced for stratifications with narrow pycnoclines, and this is precisely the regime in which we are interested. In fact, Lamb (2002) reports lack of convergence for flows with Richardson numbers (Ri) lower than $\approx$0.23, with failure to converge attributed to the intrinsic instability of the sought solutions. However, our implementation of the TEW algorithm, while maintaining the same structure, shows that convergence can be achieved at lower Richardson numbers. By adjusting some of the parameters controlling the convergence of the scheme, and improving on the stopping criterion for the iteration, we show next that accurate solutions can be determined in stratifications with narrow pycnoclines that have regions with Richardson numbers as low as 0.07.

2.1. *Numerical implementation*

We use the fast Fourier transform for the Poisson problems (2.6), (2.7) in our implementation of the TEW algorithm. First, the infinite strip domain D is truncated assuming periodicity in the horizontal direction. The period is chosen sufficiently large

to ensure adequate decay at the horizontal boundaries and the spatial discretization is chosen to be uniform. Taking advantage of the homogeneous boundary conditions at the top and bottom boundaries, we mirror the domain in the vertical direction, imposing periodic boundary conditions in both directions on the resulting domain. The equations are thus solved in Fourier space, the ensuing method being fourth-order convergent.

To evaluate the integrals (2.8)–(2.11) we use a fourth-order Simpson rule. The integrands in these expressions involve the transformation function s and its inverse (see relation (2.4)), for which two discretized look-up tables with 10^6 uniformly spaced points are pre-computed. For determining the inverse, we use a quadratic interpolation scheme. We remark that the evaluation of the integral (2.10) can be further simplified by using integration by parts and relation (2.6), which yields

$$S_3 = \int_D (\phi^k - v^k)[e_\phi(z, \phi^k) - \Delta\phi^k]\,\mathrm{d}x\,\mathrm{d}z, \tag{2.15}$$

and then by evaluating the Laplacian $\Delta\,\phi^k$ in the frequency domain.

2.2. *Stopping criterion*

The stopping criterion for the iterative scheme suggested in Turkington *et al.* (1991) ($O(10^{-3})$ in the $\mathscr{L}_2$-norm of the relative error in the eigenfunction ϕ) is not sufficient for our purposes. In fact, for stratifications with narrow pycnoclines, we found this criterion to be somewhat misleading, suggesting convergence in instances in which other tests indicate that the numerical solution is not in fact a travelling-wave solution. This can checked most directly by monitoring the (non-dimensionalized) horizontal mass flux,

$$Q(x) \equiv \int_0^H \rho\,(x, z)\,u(x, z)\,\mathrm{d}z \Big/ \int_0^H c\,\overline{\rho}(z)\,\mathrm{d}z, \tag{2.16}$$

a quantity which is conserved by a truly steady solution. As shown in figure 2(*a*), even when the $\mathscr{L}_\infty$-norm of the relative error of $\|\phi^{(k+1)} - \phi^{(k)}\|/\|\phi^{(k)}\|$ has decreased to less than 10^{-5}, the mass flux still displays significant variations along the horizontal span of the fluid domain.

Of course, the error between two successive iterations can become very small without necessarily guaranteeing that the iterating solution is within the same accuracy from the sought attractor, as simple examples of slow convergence with a progressively decreasing contraction factor readily show. Thus, apart from monitoring convergence in the relative error of the eigenfunction ϕ and the eigenvalue λ as suggested in Turkington *et al.* (1991), we also monitor the residual of the DJL equation in the transformed variable ϕ (2.5). An estimate of this residual can be constructed inside the iterative loop. Thus, by subtracting ϕ^k from relation (2.13) and applying the operator $(\alpha - \Delta)$, we obtain

$$(\alpha - \Delta)(\phi^{k+1} - \phi^k) = \frac{\mu^{k+1}}{\lambda^{k+1}}[(\alpha - \Delta)(v^k + \lambda^{k+1}w^k) + (\alpha - \Delta)\phi^k], \tag{2.17}$$

which, by using relations (2.6) and (2.7), we can rewrite as

$$(\alpha - \Delta)(\phi^{k+1} - \phi^k) = \frac{\mu^{k+1}}{\lambda^{k+1}}[-\Delta\phi^k + e_\phi(z, \phi^k) - \lambda^{k+1}f_\phi(z, \phi^k)]. \tag{2.18}$$

The right-hand side of this relation is the residual of (2.5). We note that by evaluating the residual in terms of appropriately non-dimensionalized quantities (scaling the

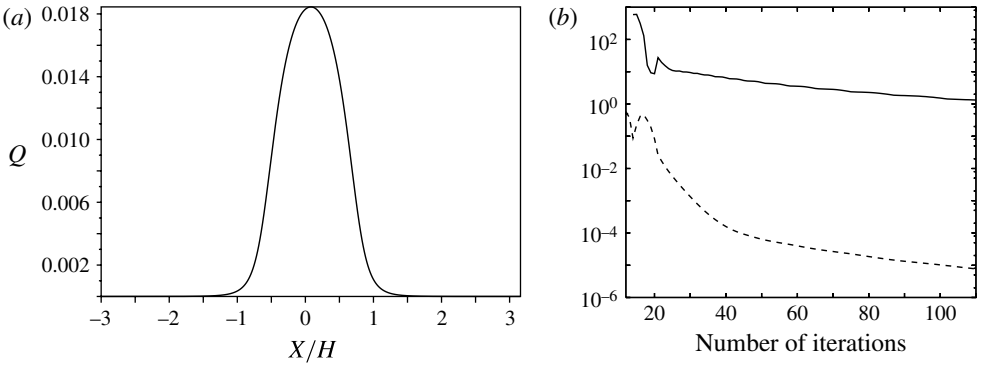

FIGURE 2. Convergence of the TEW iteration algorithm for a near-solitary travelling-wave solution in the periodic box $L = 1232$ cm, with A (non-dimensional potential energy) 3.2×10^{-3}, amplitude $a/h_1 = 1.51$, and parameters chosen as described in § 1. The resolution is 512 points in the vertical. (*a*) Horizontal mass flux $Q(x)$ after the ϕ-relative error in $\mathscr{L}_\infty$-norm becomes less than 10^{-5}; (*b*) $\mathscr{L}_\infty$-norms of ϕ-relative error (dashed line), and residual (2.18) (solid line) respectively, versus the number of iterations.

spatial coordinates with the total depth H and the velocities with $\sqrt{gH}$), the magnitude of $\Delta\phi^k$ for the pycnocline thicknesses of interest is of order 10^2. Figure 2(*b*) shows that the magnitude of the residual is substantial even when the relative error in ϕ could suggest convergence.

2.3. *Order and rate of convergence*

We have monitored the convergence of the eigenvalue λ (2.3) by fixing a threshold for the residual and looking at the relative convergence of λ while refining the discretization grid of the system. As expected, based on the fourth-order construction of all portions of the numerical scheme, the order of convergence was found to be four. The rate of convergence, however, is strongly dependent on the parameters α and β which control the convexity of the functionals involved in the iterative scheme. We note that choosing α substantially bigger than the estimate provided by relation (A 17) greatly accelerates convergence. We thus used $\alpha \approx 200$ in the majority of the numerical results presented.

The rate of convergence is also smaller when the sought solutions are strongly nonlinear, as demonstrated by figure 3, where the first figure shows the residual versus the number of iterations for three numerical solutions in the stratification (1.5) (with parameters as described in § 1) for increasing values of the parameter A corresponding to three non-dimensionalized potential energies. We remark that the minimum Richardson number corresponding to the large-amplitude wave with $A = 3.2 \times 10^{-3}$ is 0.076.

To illustrate the marked improvement in monitoring convergence based on the residual, we perform time-evolution simulations with VARDEN for two initial conditions corresponding to a solitary wave of amplitude $a/h_1 = 1.51$ (close to the maximum amplitude $a/h_1 = 1.55$ for the above choice of parameters). The first initial condition is obtained by using the stopping criterion suggested in Turkington *et al.* (1991) (namely relative error in eigenfunction ϕ of 0.001) while the other initial data are from a solution whose residual has converged to below 10^{-7}: see figure 4. Note that even though the two initial conditions are graphically indistinguishable, as

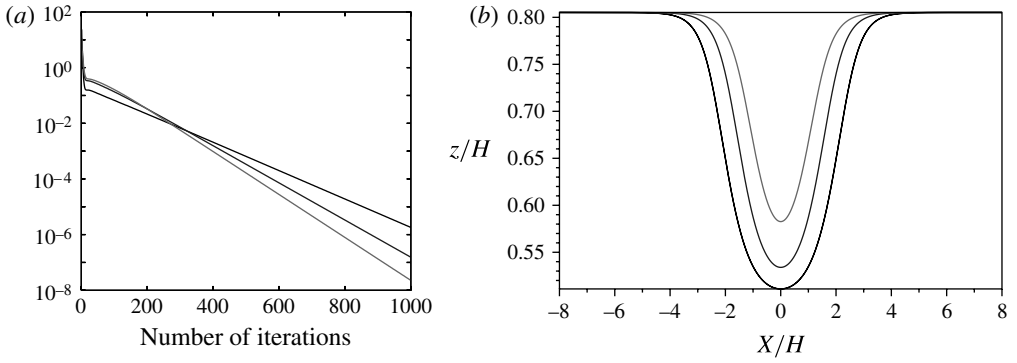

FIGURE 3. (*a*) Residual versus the number of iterations for three numerical solutions of the TEW algorithm in the stratification (1.5), with parameters chosen as described in § 1, for values of the parameter A (non-dimensionalized potential energy) of 3.2×10^{-3}, 2×10^{-3} and 10^{-3} respectively (from black to light grey). (*b*) The average density isoline corresponding to the final iteration for the three cases presented in (*a*). The computational domain is 1232 cm × 77 cm with periodic boundary conditions in the horizontal direction while the resolution is of 512 points in the vertical.

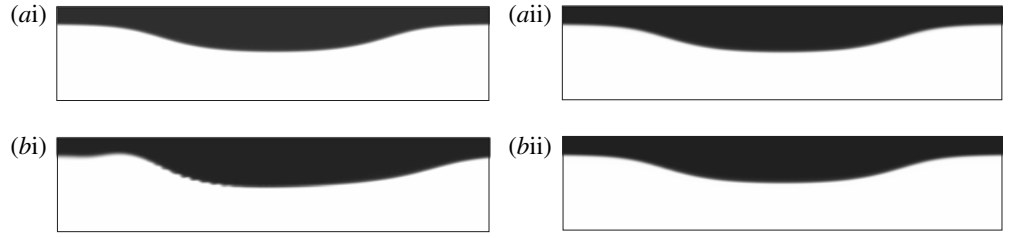

FIGURE 4. (*a*i, *b*i) Density snapshots at $t = 0$ and 15 s respectively from the time-evolution simulation for a solitary-wave solution of the TEW algorithm of amplitude $a/h_1 = 1.51$ for a solution with relative error in ϕ ($\mathscr{L}_\infty$-norm) of 0.001. (*a*ii, *b*ii) The same as above, for a converged solution, with magnitude of the residual of 10^{-7}. Only a section of the computational domain (period $L = 1232$ cm) is shown, centred at the peak of the wave, of horizontal length 300 cm, uniform scale for both x and z. The resolution is 1024 points in the vertical.

figures 4(*a*i) and 4(*a*ii) show, in the first simulation the solitary wave develops a noticeable asymmetry during its time evolution, accompanied by the manifestation of Kelvin–Helmholtz billows. Conversely, in the second simulation starting from the converged TEW solution, the wave preserves its shape symmetry, behaving as a steady wave (with no visible manifestation of shear instability). In the following section we assess in quantitative terms how far the initial condition is from a travelling permanent-form solution supported by the evolution code.

3. Validation of the evolution code

For sufficiently large amplitudes, solitary waves emerging from the experimental initialization process never fully develop into symmetric shapes and achieve travelling-wave form (Grue *et al.* 1999; Tiron 2009, §4.2). While the highly fluctuating fluid

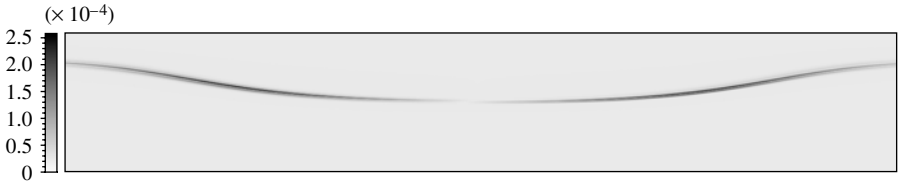

FIGURE 5. Magnitude of the relative error in the density field after 5 s, between two time-evolution runs performed at resolutions 256 and 512 points in the vertical, respectively, for a long periodic wave (near the solitary-wave limit), of amplitude $a/h_1 = 1.51$. We show here a portion from $x = 385$ cm to $x = 847$ cm of the computational domain of 1232 cm × 77 cm, uniform scale for both x and z.

motion in their wakes is travelling at a slower group speed and is eventually left behind by the large waves, its upstream influence is not clear and cannot be completely ruled out, as evidenced by the slightly asymmetric shape of the precursor large wave. In order to assess whether this asymmetry originates in the initial conditions or is related to an inherent instability of large waves, we seek to initialize the evolution code with a permanent-form solitary-wave solution. The boundary conditions for the evolution code are zero vertical velocity at the top and bottom boundaries and periodic in the horizontal direction. We use the single-grid version of the code with isotropic spatial discretization and the time step selected by enforcing the Courant–Friedrichs–Lewy condition: see Puckett *et al.* (1997) and Almgren *et al.* (1998) for details. We initially perform our study on a long *periodic* wave (near the solitary-wave limit) with period $L = 1232$ cm and large amplitude ($a/h_1 = 1.51$). There are two interconnected issues that we address in this section: one is the convergence of the evolution code itself for large density gradients, and the second is the correctness of the initialization, namely how far the initial condition is from a travelling-wave, permanent-form solution supported by the evolution code. We remark that the first issue can be analysed without reference to any DJL internal wave solution, by simply focusing on parallel shears where a spectral study can be carried out essentially in closed form, with growth rates of most unstable modes determined with arbitrary accuracy. This is taken up in § 4.2 and again in appendix B.

We have tested the order of convergence of the evolution code both for initialization with experimental set-ups (starting from an initial step in density) and for solitary-wave initializations. For the first case, we obtain first-order convergence – as expected due to the lack of smoothness of a step initial condition. Second-order convergence of the evolution code is achieved in the case of smooth initial conditions by initializing with a solitary-wave solution obtained with the iterative scheme (Turkington *et al.* 1991), with a square grid at the (vertical) resolution $N = 1024$, and running three time-evolution simulations at resolutions $N = 256$, 512 and 1024, respectively. We have monitored the $\mathscr{L}_\infty$-norm of the error in the velocity and density fields. The numerical errors concentrate in the pycnocline region, where we register the highest gradients of density: see figure 5. This figure also reveals that part of the initial error lies simply in the travelling-wave speed, which varies slightly with the resolution used in the evolution code for the same initial condition. Furthermore, an additional source of this error is the difference in speed between the TEW iteration code solution and that supported by the time-evolution code for a (near) solitary wave of the same amplitude. In fact, the structure of the error depicted in figure 5 can clearly be ascribed to a small

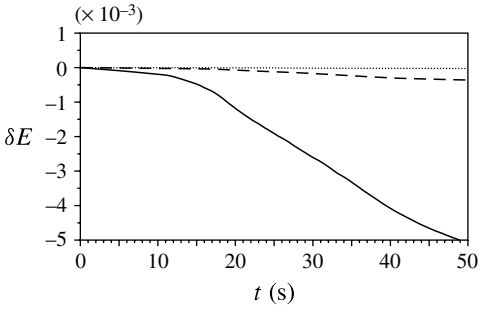

FIGURE 6. Variation of the total energy for the time evolution of the wave of amplitude $a/h_1 = 1.51$ (normalized with the energy at time $t = 0$ s). Solid line, resolution $N = 256$ points in the vertical; dashed line, $N = 512$; dotted line, $N = 1024$. The computational domain is 1232 cm × 77 cm.

overall horizontal shift in the wave position occurring at short times. This horizontal shift error decreases with increasing resolution at any given time. Of course, this observation also partially addresses the second issue mentioned above, i.e. closeness of the initial condition to a wave of permanent form supported by the evolution code. Another indicator of the magnitude of the numerical error induced by the sharp stratification is the total energy: this should be conserved in our set-up (periodic boundary conditions in horizontal direction, slip in the vertical). Figure 6 shows the variation of the total energy for three resolutions $N = 256, 512, 1024$, respectively. We note that while the total energy decays in time due to numerical diffusion, this decay is smaller for finer resolutions, and the choice of $N = 1024$ is adequate for most time scales of interest.

Conservation of energy also pertains to the closeness issue of the TEW initial condition to waves of permanent form for the evolution code. Monitoring the wave amplitude, the phase speed and the potential and kinetic energy separately further addresses this issue, as all of these quantities should be constants of motion for a steady travelling wave. As we see in figure 7, the time variation of these quantities decreases significantly with increasing resolution.

4. Instability study

In this section we embark on the stability study of solitary-wave solutions obtained with the TEW code described in § 2. Specifically, in § 4.1 we look at the self-induced shear instability of these solutions during their time evolution and the role played by the resolution used in the evolution code. Next, in § 4.2 we perform a local stability analysis of the solitary wave, while in § 4.3 we discuss local versus global stability of internal wave solutions. In § 4.4 we derive and test a simple envelope equation for the amplitude of unstable growth based on the local stability analysis. Then, in § 4.5 we provide stability estimates from strongly nonlinear long-wave models, and in § 4.6 we employ these estimates to determine an amplitude threshold for manifestation of shear instability.

4.1. *Self-induced instabilities*

We focus on the case of the solitary wave of near-maximum amplitude $a = 1.51$, which we used in the validation study above. We found evidence of shear instability

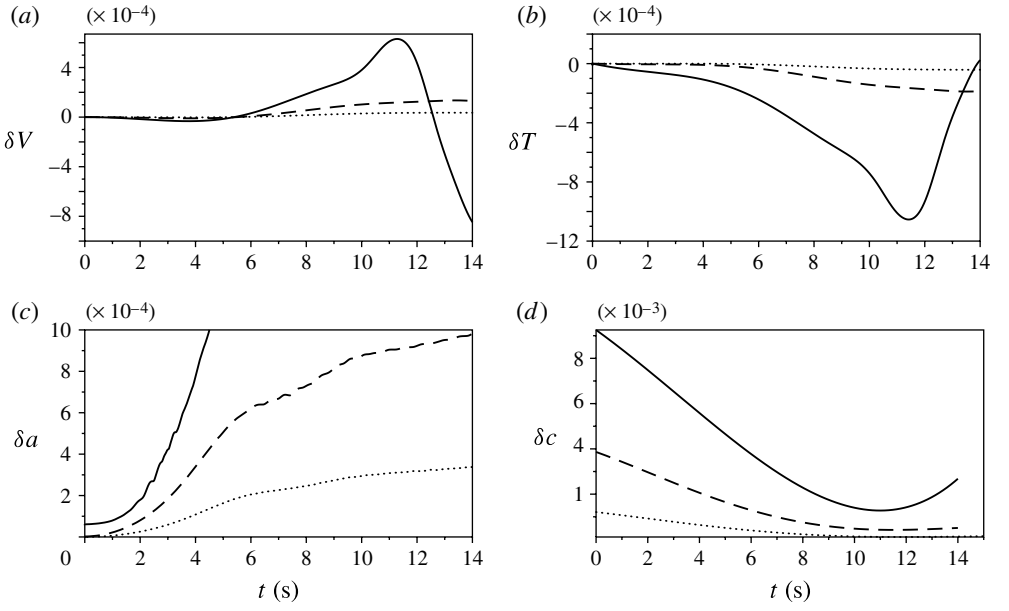

FIGURE 7. Variation of (*a*) potential energy, (*b*) kinetic energy, (*c*) amplitude, (*d*) phase speed for the time evolution of the wave of amplitude $a/h_1 = 1.51$. Solid line, resolution $N = 256$; dashed line, $N = 512$; dotted line, $N = 1024$. All quantities are non-dimensionalized with the corresponding quantities at time $t = 0$ s.

for all the resolutions tested, as can be seen in figures 8–9, where we present several time snapshots of the density field during the evolution of the wave. (The simulations presented are performed in the wave frame, a frame of reference moving at the speed c_{wave}, the speed of the wave as predicted by the TEW code.) Nonetheless, the magnitude of the roll-ups decreases with increased resolution (to the point that they are not easy to identify visually, as the inset of figure 9*c* shows), which can be interpreted as yet another confirmation of convergence of the iterative code to actual travelling-wave solutions of the Euler equations. Moreover, the instabilities are manifested only on the trailing side of the wave, as also noticed in experiments (Grue *et al.* 1999; Fructus *et al.* 2009).

In all three simulations, we have observed (qualitatively) three episodes of shear instability: an initial episode triggered by numerical error (followed by a period in which the wave travels at quasi-constant speed and amplitude), a second episode of instability of smaller magnitude (which occurs roughly in the interval 30–40 s) and finally the interaction with the wake created by the first episode, which wraps around the periodic box: see figure 8 for resolutions $N = 256$, where the first two episodes are clearly visible, and $N = 512$, where the second episode is barely discernible in the density field (the inset of figure 8*f*(ii) magnifies the region where growing modes are detected).

We argue that the simulations, at all the resolutions we have tested, retain important physical features of the actual phenomenon. Thus, the first episode of instability is induced by numerical error in both the evolution code and the initial condition, which can be viewed as an *initial perturbation* superimposed on the travelling-wave solution of the discrete operator associated with the evolution code. (We stress that

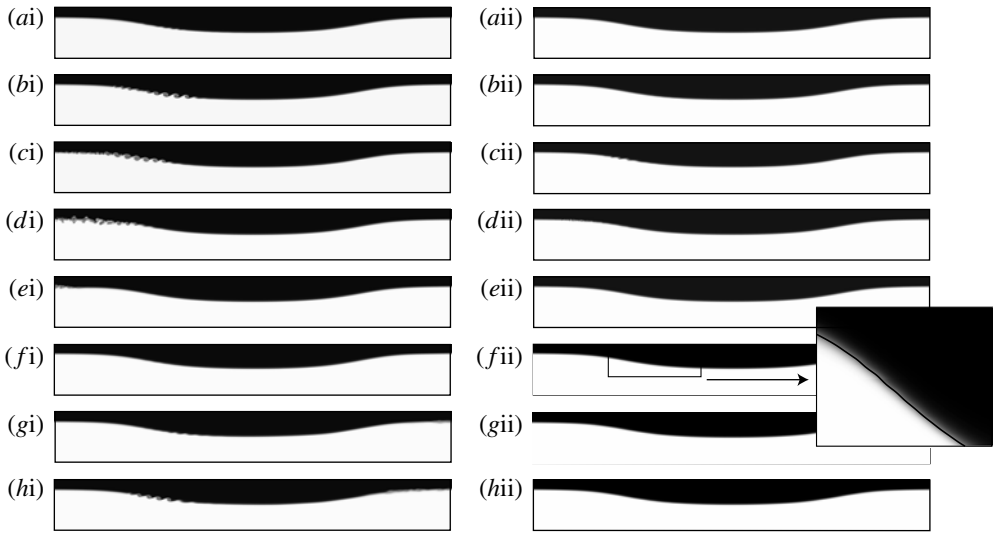

FIGURE 8. (*ai*–*hi*) Time snapshots of the density field at (*a*) 8, (*b*) 12, (*c*) 16, (*d*) 20, (*e*) 26, (*f*) 40, (*g*) 45 and (*h*) 50 s during the propagation of a large-amplitude internal wave with $a/h_1 = 1.51$. Only a window of the computational domain (period $L = 1232$ cm) is shown, centred at the peak of the wave, with horizontal length 300 cm, uniform scale for both x and z. (The simulation is performed in the wave frame moving at the speed c_{wave}, the speed of the wave as predicted by the TEW code.) Resolution is 256 points in the vertical. (*a*ii–*h*ii) The same as above, for a resolution of 512 points in the vertical.

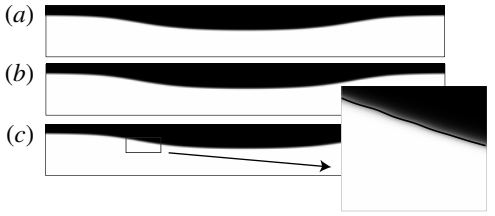

FIGURE 9. The same as figure 8 (at (*a*) 8, (*b*) 12, (*c*) 16 s), resolution 1024 points in the vertical.

this perturbation is due to numerical errors, in contrast with the perturbations used later on, which will be seeded to target maximum growth rates of shear instability.) Simultaneously with the growth in the unstable region of the wave, this perturbation is shed downstream (in the wave frame), and starts propagating in a stable region of the flow field. The shear in this region on the downstream side of the wave decays to zero exponentially fast for solitary waves, with the density stratification limiting to that of the quiescent state. The perturbation therefore propagates mainly as a dispersive (weakly nonlinear for sufficiently large time) wave train governed by the dispersion relations determined by the background stratification. It can be shown that in the frame of reference of the wave, all normal modes in this region are travelling from right to left, both their phase speed and group velocity being thus bounded below by $c_0 - c_{wave}$ and above by $c_0 + c_{wave}$, where c_0 is the linear long wave speed (*critical speed*) in

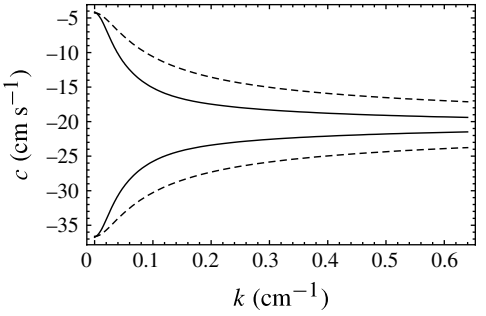

FIGURE 10. The two branches of the dispersion relation for the background stratification (1.5). Group velocity (solid line) and phase speed (dashed line) (both in the frame of the wave of amplitude $a/h_1 = 1.51$ travelling with speed $c_{wave} \approx 20.44$ cm s^{-1}), as function of the wavenumber.

the background stratification and c_{wave} is the speed of the wave (with $c_{wave} > c_0$): see figure 10 for the two branches of the dispersion curves. We will return to this fact and its implications for stability later on in this section.

We remark that all time-dependent simulations for propagation of solitary-wave solutions (regardless of whether shear instabilities occur or not) exhibit a wake in the pycnocline region, which is visible in both the density and the velocity fields. Its magnitude decreases with resolution, indicating that the wake is a result of a downstream-shed initial perturbation. In fact, we can identify qualitatively the superposition of normal modes of the background stratification in the velocity field associated with the wake: see figure 11. Of course, for a rigorous quantitative comparison of the normal modes with the features in the wake, knowledge of the exact form of the initial perturbation would be needed. However, as shown in figure 11(*c*), from the dispersive wave train, the fastest travelling normal mode wrapping around the period-box would emerge first. Thus, we argue that the second episode of instability is triggered by the fastest travelling normal mode of the background stratification (which travels with a group velocity bounded above by $c_0 + c_{wave}$) and it is not part of the instability triggered by the initial evolution of the perturbation.

We test this conjecture by doubling the length of the computational domain, thus initializing the evolution code with a long periodic wave solution of the TEW code, with double the period and the same amplitude and speed. We perform simulations at the resolution $N = 512$. Since, for this resolution, the shear instability is not immediately apparent in the density field, we monitor and display the horizontal pressure gradient. In figure 12 we show the horizontal pressure gradient at time $t = 50$ s for both the wave of period $L = 1232$ cm and of period 2464 cm, respectively. Note that the wave with period 2464 cm does not exhibit a pressure mark of instability, as opposed to the wave of shorter period. In fact, we can estimate the minimum time of travel of the fastest normal mode above as $(c_0 + c_{wave})/L$, where L is the period. In particular, for the long wave of period $L = 1232$ cm (taking into account that the critical speed c_0 is $\approx$16 cm s^{-1}, whereas the speed of the wave c_{wave} is $\approx$20.44 cm s^{-1}) this estimate is $\approx$34 s, which falls in the range 30–40 s observed in the simulations.

All numerical experiments we have performed suggest, apart from the convergence of the steady solution, some interesting stability properties of the flow. In the limit of an infinite period, the internal waves investigated would be globally linearly stable

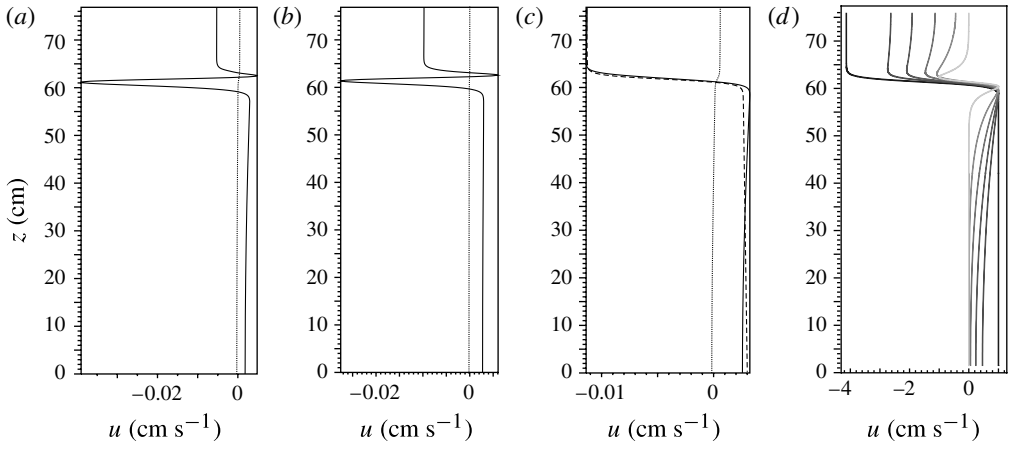

FIGURE 11. Horizontal velocity profiles (in the laboratory frame) at times $t = 0$ (dotted line) and $t = 17.5$ s (solid line) for an evolution simulation of a wave of amplitude $a/h_1 = 1.51$ and period $L = 1232$ cm, measured at (*a*) $X = 50$ cm, (*b*) $X = 100$ cm from the left end of the computational domain and at (*c*) $X = 100$ cm from the right end respectively. (The simulation is performed in the wave frame moving at the speed c_{wave}, the speed of the wave as predicted by the TEW code, with a resolution of 512 points in the vertical.) It can be inferred that the perturbation left behind the wave wraps around the periodic computational domain and the first to emerge here is the fastest travelling normal mode of the background stratification (represented with dashed line in *c*). (*d*) Horizontal velocity profiles for normal modes of the background stratification with wavenumbers ranging from 0 (black) to 0.4 cm^{-1} (light grey).

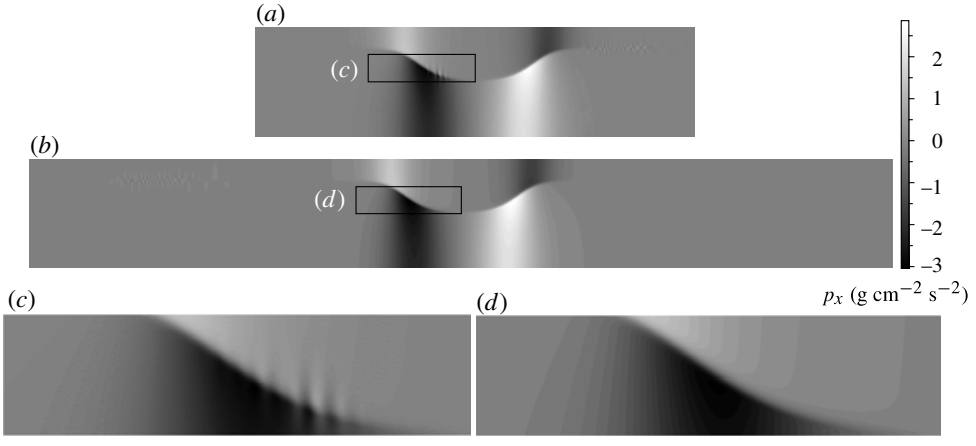

FIGURE 12. Horizontal pressure gradient p_x at time $t = 50$ s from the time evolution of two waves of the same amplitude $a/h_1 = 1.51$, with periods (*a*) $L = 1232$ cm and (*b*) $L = 2464$ cm. Both simulations are performed in the wave frame, moving at the speed c_{wave}, the speed of the wave as predicted by the TEW code, with a resolution of 512 points in the vertical. In both cases the entire computational domain is shown, displayed here with modified vertical-to-horizontal scale ratio 4:1.

since the initial perturbation (after some growth in the unstable region located at the peak of the wave) is advected away, leaving the wave in an equilibrium state, close to

the unperturbed solitary wave, possibly after compensating for horizontal translations, as appropriate for orbital stability of travelling waves (see e.g. Benjamin 1972 for the exemplary case of the Korteweg–de Vries equation). For a finite period, however, the dispersive train generated by the first episode of instability wraps around the periodic box potentially triggering subsequent episodes of shear instability. It is tempting to conjecture that such periodic travelling waves, as time progresses, would relax to a state where the dispersive wave trains no longer excite shear instabilities, by effectively stirring the pycnocline region to a larger thickness and possibly reducing the amplitude of the wave by transferring its energy to different modes. Such a state could ultimately be independent of the magnitude and nature of the initial perturbation, and would depend on the background stratification only, thus indicating overall instability of the original wave train. In the following section, in order to shed some light on these observations, we examine in detail the local spectrum of the self-induced shear flow.

4.2. *Local stability analysis of the solitary-wave solution*

As argued before, both the shear and the density stratification of the solitary wave have slow variation in the horizontal direction, hence the first-order approximation reduces to the case of a parallel stratified shear flow. Linearizing the Euler equations (1.1)–(1.4) with respect to small perturbations of the basic parallel shear flow $u_0(z)$ with stratification $\rho_0(z)$ and assuming that any perturbation can be decomposed in independent wave components leads to the linear eigenvalue problem for the stability problem (often referred to as Taylor–Goldstein equation)

$$\psi'' + \frac{\rho_0'}{\rho_0}\psi' - \left[\frac{\rho_0'}{\rho_0}\frac{g}{(u_0-c)^2} + \frac{(\rho_0 u_0')'}{\rho_0(u_0-c)} + k^2\right]\psi = 0, \tag{4.1}$$

where $\psi(z)$ is the magnitude of the perturbation stream function and k, c are the wavenumber and phase speed of the perturbation, respectively. The boundary conditions for a flow confined between two rigid walls at 0 and H are

$$\psi(0) = \psi(H) = 0. \tag{4.2}$$

Note that the form (4.1) of the Taylor–Goldstein equation we use retains the stratification contribution to inertia; the term ρ_0'/ρ_0 in the coefficient of ψ' is often dropped in the so-called Boussinesq approximation of neglecting the fluid's inertia. The papers by Long (1965) and Benjamin (1966) warn about the use of this approximation in (large) internal wave studies, and we avoid the approximation throughout this work. We also remark that the influence of viscosity on the stability properties is expected to be minimal, slightly reducing the growth rates, as confirmed by our numerical investigations of viscous shear flows (not reported here) and in agreement with Maslowe & Thompson (1971), who show that the viscosity effects on the maximum growth rates are very small for Reynolds number above 100. We recall that for our set-up, which refers to an experiment with stratified water, typical Reynolds numbers would be $uL/\nu \approx 5 \times 10^5$, where $\nu = 10^{-6}$ m^2 s^{-1} is the kinematic viscosity and the length scale L is given by the characteristic wavelength of the solitary wave ($\approx$500 cm), while the characteristic velocity u corresponds to the maximum fluid velocity ($\approx$10 cm s^{-1}).

Since our principal aim is to investigate the mathematical stability (in the Lyapunov sense) of travelling solitary-wave solutions, in what follows we focus on the *temporal* evolution of an initial perturbation superimposed on the base flow. The temporal evolution approach is the most appropriate for this particular viewpoint, which naturally focuses on the real wavenumber case through an initial condition

perturbation. Hence, (4.1) is solved with boundary conditions (4.2), for fixed real wavenumber k and phase speed $c = c_R + \mathrm{i}c_I$ as the eigenvalue. In this interpretation the eigenvalue problem is non-symmetric, and hence in general c can be complex. The flow is unstable if $c_I > 0$, and the associated normal mode has the rate of growth $\omega_I = kc_I$. We note that (4.1) becomes singular for c real and in the range of u_0. Eigenvalues c with this property are singular neutral modes, and correspond to the boundaries of linear stability.

We solve (4.1), with boundary conditions (4.2), by employing a shooting method similar to the one in Hazel (1972). For fixed wavenumber k, we integrate from the centre of the pycnocline location z_p to left and right by imposing continuity of both the eigenfunction ($\psi_L(z_p) = \psi_R(z_p) = \psi_p$, with ψ_p a normalization constant for the eigenfunction) and its derivative in the centre ($\psi'_L(z_p) = \psi'_R(z_p) = \psi'_p$). We thus define two functions depending on the slope of the eigenfunction ψ'_p and on the eigenvalue c. We determine the eigenvalue c and the slope of the eigenfunction by imposing the boundary conditions (4.2), and by solving the corresponding nonlinear system. Unlike Hazel (1972), we choose to integrate from the centre of the pycnocline outwards in order to control the magnitude of the eigenfunction. In order to locate numerically all unstable modes, we search within a domain of the complex c-plane identified by the *semicircle theorem* of Howard (1961), i.e. the semicircle in the upper half-plane of the complex c-plane which has as diameter the range of the horizontal shear. We have detected a single unstable branch for all configurations investigated, as expected based on the general principles for the stratification we use (Miles 1963). In fact, the evolution code captures rather well both the growth rate and the phase speed of these linear normal modes: see appendix B, where we present a comparison of the time evolution of normal modes predicted by the linear theory and numerical solutions with VARDEN. These tests are performed for a parallel shear constructed with the velocity and density profile from the maximum displacement of the large amplitude wave $a/h_1 = 1.51$, computed with the TEW algorithm. Detailed spectrum calculations are presented next for this large-amplitude wave $a/h_1 = 1.51$. The local unstable spectrum is computed by 'parallelizing' the shear flow of this solution for a series of horizontal locations in between the point of maximum displacement of the wave and the end of the region of potential instability $Ri < 1/4$ (noting that both the horizontal velocity and the density stratification are symmetric with respect to the point of maximum displacement): see figure 13, where we show a contour plot of the Richardson number for the area of potential instability. All the stability computations are performed in the frame of reference of the wave (moving at horizontal speed c_{wave} with respect to the fixed-laboratory frame).

In figure 15 we show the phase speed of the unstable modes for the eight combinations of shears and density stratifications shown in figure 14. Note that the phase speed of the normal modes is negative, and moreover it decreases for increasing k, which implies that the group velocity ($\mathrm{d}\omega_R/\mathrm{d}k$) is also negative. Next, we illustrate the dependence of the unstable spectrum on the horizontal location across the region of local instability. First, we note that the normal mode that would first be visible in the evolution of a perturbed initial state can be expected to correspond to the mode with the maximum growth rate. We expect this to be the case as long as the horizontal extent of the area of local instability is larger than the periods associated with these modes, which is the case for most of the waves considered in this study. From figure 16(a) we can infer that the wavenumber associated with the most unstable mode does not vary significantly along the wave profile. Furthermore, in figure 17, we can

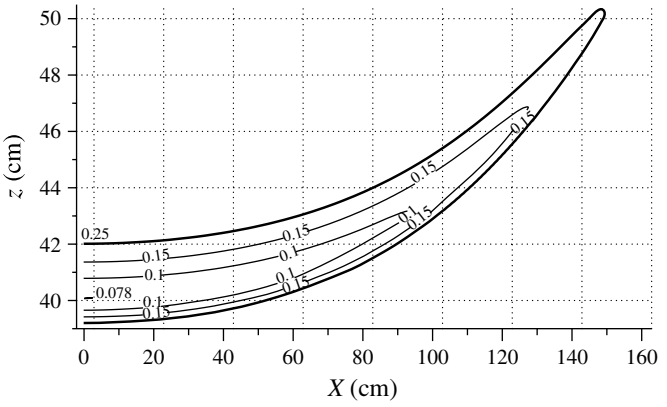

FIGURE 13. Contour lines of the Richardson number in the region of potential instability (half of the region represented with altered aspect ratio) for a wave of amplitude $a/h_1 = 1.51$. The horizontal extent of (half of) the region where $Ri < 1/4$ is 155.3 cm.

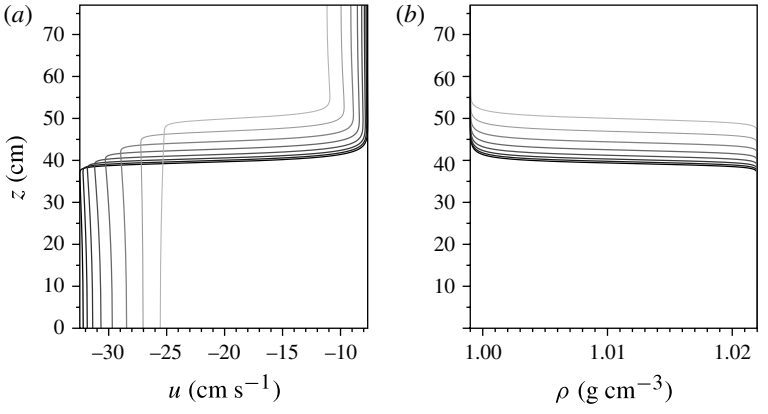

FIGURE 14. (*a*) Horizontal velocity profiles, (*b*) density profiles for the wave from figure 13, at eight equidistant locations in between $X = 0$ cm (the peak of the wave) and $X = 134.75$ cm (close to the end of the area of $Ri < 1/4$).

see that the period of the self-induced shear instability for an actual wave evolution falls in the range predicted by the local eigenvalue calculation (12.69–14.27 cm).

In figure 16(*b*) we show the variation of the growth rate associated with the most unstable normal mode in the horizontal direction. Note that the horizontal range of *potential* local instability corresponding to $Ri < 1/4$ (2×155.3 cm) almost coincides with the range of *actual* local instability (2×153.8 cm). Finally, in figure 16(*c*) we show the phase speed and the group velocity associated with the most unstable mode, which is negative at all horizontal locations in the region of local instability. This fact explains at first order the behaviour described in § 4.1, namely the initial perturbation located at the peak of the wave grows and it is advected away from the pocket of instability. This advection allows for further classification of internal wave stability, which we briefly review next.

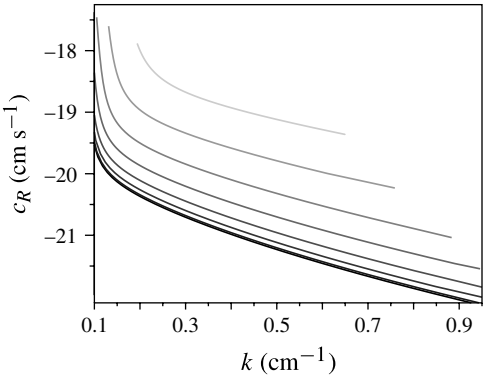

FIGURE 15. Phase speed of the unstable branches versus the wavenumber for the eight parallel shears constructed with the density and horizontal velocity profiles from figure 14. Black, $X = 0$ cm; light grey, $X = 134.75$ cm.

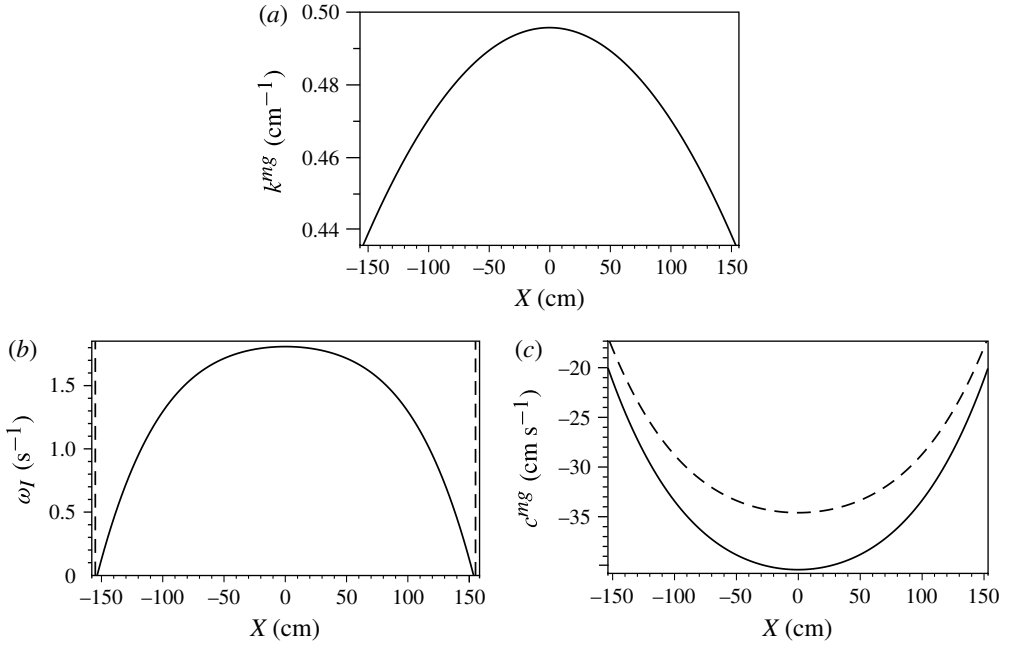

FIGURE 16. (*a*) Wavenumber corresponding to the maximum growth unstable mode along the wave profile for the wave represented in figure 13. (*b*) Maximum growth rate along the wave profile. (*c*) Phase speed (dashed line) and group velocity (solid line) associated with the maximum growth rate along the wave profile. The thin vertical dashed lines mark the range of the region of potential local instability, $Ri < 1/4$, whose (half) horizontal extent is 155.3 cm, while the (half) horizontal extent of the region with non-zero imaginary component of c is 153.8 cm.

4.3. *Local versus global stability of internal wave solutions*

Relatively recent advancements in the stability theory of spatially varying flows as presented in Huerre & Monkewitz (1985, 1990) and Huerre (2007), based on slowly

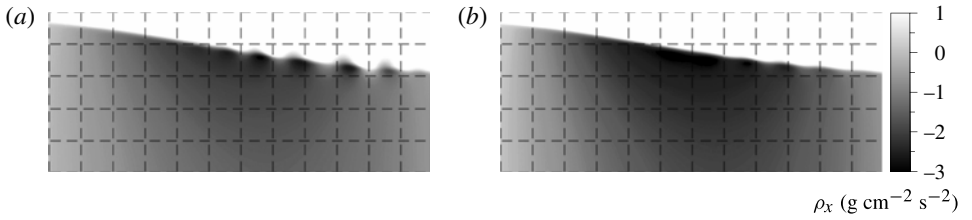

FIGURE 17. Portion of the horizontal pressure gradient p_x (located at the left of the peak of the wave) from the time-evolution simulation of the wave of amplitude $a/h_1 = 1.51$ and period $L = 1232$ cm at resolutions (*a*) 512 and (*b*) 1024 respectively. The snapshot is taken at $t = 11$ s in both cases. Superimposed on each plot is a grid with spatial resolution of 10 cm, to show the characteristic wavelength of the self-induced instability.

varying asymptotics (WKBJ analysis), shed some light on the class of self-induced instabilities in internal wave propagation. The approach assumes *scale separation*, i.e. the streamwise variation of the flow must be slow over a typical wavelength of the perturbation, so that the local dispersion relation can be used in the global stability analysis of the flow, as a leading-order approximation. We note that the internal wave flows we are studying appear to meet these requirements.

The foundation of the approach of Huerre & Monkewitz (1985, 1990) and Huerre (2007) lies in the fundamental distinction between *absolute* and *convective* instability (see also Briggs 1964). A parallel shear flow is said to be convectively unstable if the growing wave train generated by an initial perturbation is advected away. Conversely, the flow is said to be absolutely unstable if the instability contaminates the entire medium. This distinction seems trivial in the case of strictly parallel stationary flows, which are frame-invariant: a simple change of frame of reference renders a convectively unstable parallel flow into an absolutely unstable one. However, when considering spatially developing stationary flows, these concepts become relevant, since the frame of reference in which the flow is stationary is singled out. The main conjecture of the theory is that a necessary (although not sufficient) condition for the existence of time-periodic intrinsic oscillations (or self-sustained global modes) is the existence of a pocket of *absolute* instability somewhere in the flow field.

The flow considered here appears to have a pocket of *convective* instability (as evidenced by the *negative* group velocity of the local spectrum in the region of local instability and supported by the time-dependent simulations), while being locally stable outside this region. Thus, in the framework of the theory described above, this flow does not support self-sustained global modes – a conjecture supported by the numerical simulations.

We remark that the term 'convective' is also used in the literature to qualify another mechanism of wave breaking that occurs when the fluid velocity approaches the phase speed of the wave, or equivalently the fluid is stationary in the frame of reference of the wave (see for instance Holyer 1979). The waves investigated in this work do not exhibit this property and thus throughout the remainder of this paper we employ the term convective only in the context described in the paragraph above.

We also remark that throughout this work we focus on the temporal, or initial-value, stability problem, as opposed to time-signalling stability, whereby a time-dependent perturbing forcing term is applied at some spatial location for all forward times. A natural setting for such a signalling problem is that of a time-periodic perturbation added to the upstream (constant) flow in the reference frame in which the wave

appears stationary (as in Lamb & Farmer 2011). However, such a set-up (which essentially corresponds to a boundary forced problem since the upstream boundary conditions are *de facto* assigned) is conceptually different from the case we are focusing on: that of a freely propagating wave, which would change its energy and hence its physical parameters (such as its velocity) in response to perturbations, in a time-dependent fashion. In order to make the time-signalling approach relevant to the free wave case, one would need to implement some sort of feedback loop to modify the upstream boundary conditions according to the system's response in the wave frame.

The mathematical scenario emerging from the results of the last two sections on the stability properties for solitary internal waves can be summarized as follows. For solitary waves with an instability pocket centred at their peaks, localized initial perturbations grow in the region around the peak where the local unstable shear is strongest and supports the highest growth rates of the unstable mode. Because the instability appears to be convective, perturbations are swept away from the peak region, with the wave reaching a state of local equilibrium afterwards. Thus, for localized perturbations, the finite extent of the unstable shear region (which for thin pycnoclines essentially coincides with the region where $Ri < 1/4$) combined with the convective nature of the instability would ensure that the bulk of the travelling wave flow returns to a balanced state. Mathematically, in truly laterally unbounded domains, it can then be conjectured that internal travelling-wave solutions of the stratified Euler system (1.1)–(1.4) are stable in the sense of Lyapunov (see e.g. Arnold 1992). Accordingly, measured with an appropriate norm in functional space, the distance between an exact internal wave solution and its perturbation should scale for all times as a vanishing function of the initial distance. This is because the growth of localized initial perturbations is limited to the time of residence in the instability pocket, which is a function of the associated phase and group velocities of normal modes. Hence it should always be possible to control the time evolution of a normed measure of the perturbation by its initial magnitude measured in the same functional norm, which is essentially the definition of Lyapunov stability.

As already remarked above, this mathematical scenario of stability might not apply to *periodic* internal wave trains, where instability pockets would be strung periodically throughout the flow domain, thus allowing for convective perturbations to revisit unstable regions for all times. However, there might be mathematical subtleties associated with this scenario, as the dynamics between unstable pockets might strip an evolving perturbation of its unstable modes, thereby again reaching a balanced state whose distance, in some functional norm, from the periodic solution is controlled by the initial perturbation size. Moreover, the stability of periodic wave trains is likely to be affected by a version of the Benjamin–Feir instability just as for their free-surface counterparts. Finally, we remark that the case of sufficiently nonlinear conjugate states whereby the instability pocket would extend to infinity downstream of the front should provide an actual unstable solution of system (1.1)–(1.4) in the strict mathematical sense of Lyapunov, as any localized upstream perturbation would eventually reach an unbounded domain of convectively unstable shear flow, leading to growth which could not be controlled by the magnitude of the initial perturbation. Of course, none of these considerations can be made rigorous without a precise definition of a functional norm with which the distance between solutions of (1.1)–(1.4) can be measured, which is likely to constitute a substantial mathematical task, as noted by Benjamin (1986).

While Lyapunov stability is mathematically relevant, a fluid dynamics perspective in the classification of different types of instability might be more useful in applications, and we turn next to introducing some simple tools to this end.

4.4. *Simple envelope equation for instability*

In the experimental investigations of Grue *et al.* (1999) and Fructus *et al.* (2009), as well as in the numerical simulations of a number of authors (Barad & Fringer 2010; Carr *et al.* 2011; Lamb & Farmer 2011), Kelvin–Helmholtz roll-ups invariably develop *after* the point of maximum displacement of the wave, with no growth observed in the front of the wave. This spatial asymmetry of the instability can be explained in part by its *convective* nature, which imparts a growth rate to a downstream moving wave packet (in the wave reference frame). However, the details of asymmetric growth may involve a more subtle dynamics, as the analysis of the shear and the direct numerical simulation we present next seem to suggest.

We use the local spectrum calculation developed in the previous section to construct a simple envelope equation for the perturbation evolution in the unstable region, and compare it qualitatively to numerical simulations, following the same strategy as in Troy & Koseff (2005). An estimate of the time of travel of the perturbation in the unstable region, denoted by T_w, can be constructed based on the length of the area of local instability and the speed of propagation of instability. However, because the shear flows generated by internal (long) wave motion are (slowly) varying in the horizontal coordinate X, both the phase speed and the group velocity of the vertical normal modes vary along the unstable region (up to $\sim$10 % of the speed of propagation of the wave). In an attempt to include the spanwise variation of both the phase speed and of the growth rate of the most unstable mode, we propose the following envelope equation for the evolution of a monochromatic perturbation with wavenumber close to the maximum growth rate normal mode (as predicted by the local stability analysis)

$$A_t + c_R(X)A_X - \omega_I(X)A = 0, \tag{4.3}$$

where $A(X, t)$ is the amplitude of the perturbation, $c_R(X)$ is the phase speed (the appropriate quantity for a monochromatic train) corresponding to the maximum (with respect to wavenumber k) growth rate at location X and $\omega_I(X)$ is the maximum growth rate at location X. No attempt is made here to follow the dispersive evolution in both (slow) time and space of the wavenumber and frequency of the perturbation normal modes; however, by considering only maximal quantities this model can serve the purpose of illustrating how a crude approximation of convectional unstable growth may not fully account for the observed instability in the $Ri < 1/4$ pocket of wave-induced shear around the maximum pycnocline displacement. A more detailed mathematical approach would ultimately be needed to model the unstable evolution. We solve (4.3) by the method of characteristics. We denote the length of the region of local instability by $\widetilde{L}$, and place the coordinate system origin at the point of maximum displacement of the pycnocline. Then the time of travel of a perturbation across the instability region is

$$T_w = F(\widetilde{L}/2) - F(-\widetilde{L}/2), \tag{4.4}$$

where

$$F(X) = \int \frac{1}{c_R(X)}\,\mathrm{d}X. \tag{4.5}$$

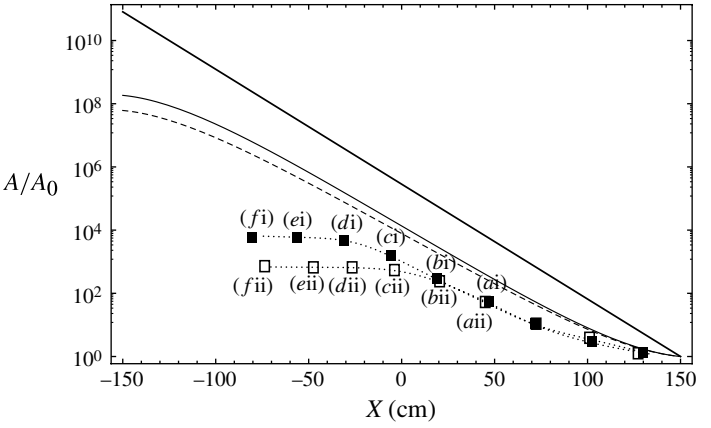

FIGURE 18. Amplification factor (A/A_0) for a perturbation initiated at the right boundary of the instability region. Thin solid line, calculated by accounting for the spatial variation of the phase speed and growth rate of the most unstable local mode; dashed line, calculated by replacing the phase speed with the group velocity; thick solid line, calculated by approximating both the local growth rate and the local phase speed with the corresponding values at the maximum displacement. The data points correspond to the two VARDEN simulations described in figure 19: filled squares, initial magnitude of the perturbation in stream function of 0.01 cm^2 s^{-1}; empty squares, magnitude of 0.1 cm^2 s^{-1}.

The characteristic curve initiating at the right boundary of the instability region is parametrized by $\{[X(s) = s, t(s) = F(s) - F(\widetilde{L}/2)] : -\widetilde{L}/2 < s < \widetilde{L}/2\}$, and the amplitude of the perturbation along this characteristic is

$$A(X, t(X)) = A_0(\widetilde{L}/2) \exp\left[\int_{\widetilde{L}/2}^{X} \frac{\omega_I(s)}{c_R(s)}\, \mathrm{d}s\right], \quad X \in [-\widetilde{L}/2, \widetilde{L}/2]. \tag{4.6}$$

In figure 18, we show the amplification factor A/A_0 for the wave of amplitude $a/h_1 = 1.51$, computed by: (i) taking into consideration the spatial variation of both the phase speed and growth rate pertaining to the dominant unstable mode; (ii) replacing the phase speed of the dominant local unstable mode with its group velocity; and (iii) approximating both the phase speed and the growth rate with the corresponding values at the peak of the wave. Note that replacing the phase velocity with the group velocity yields a smaller but comparable amplification rate across the unstable region. On the other hand, using exclusively the growth rate and phase velocity of the dominant unstable mode at the peak of the wave leads to over-prediction of the amplification by several orders of magnitude. The amplification factor at the peak of the wave predicted by this simple model for the large-amplitude wave $a/h_1 = 1.51$ is substantial (10^4). Hence, for a perturbation entering the unstable region from the front of the wave, we expect to see appreciable growth at this particular point. We remark, however, that in both experiments (Grue *et al.* 1999) and time-evolution simulations of solitary-wave solutions (in § 4.1, see in particular figure 8) no significant growth is noticeable at the point of maximum displacement, and practically no growth is detected in the front of the wave's maximum-amplitude point. We also remark that, in agreement with the findings of Carr *et al.* (2011), our studies of amplification prove to be sensitive to the details of the shear flow, making simplistic models of amplification somewhat inaccurate.

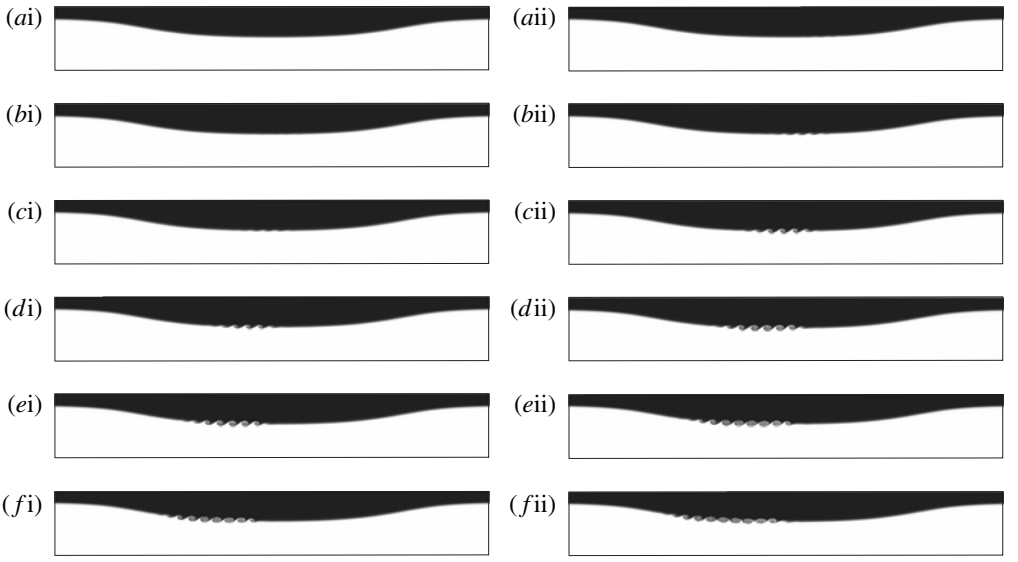

FIGURE 19. (*a*i–*f*i) Time snapshots of the density field at (*a*) 9.9, (*b*) 11, (*c*) 12, (*d*) 13, (*e*) 14 and (*f*) 15 s during the propagation of a large-amplitude internal wave with $a/h_1 = 1.51$, seeded with an initial perturbation in the stream function of magnitude 0.01 cm^2 s^{-1}. The perturbation has wavenumber 0.5 cm^{-1} and is initially situated in front of the wave (259 cm with respect to the maximum displacement of the wave). Only a section of the computational domain (period $L = 1232$ cm) is shown, centred at the peak of the wave, of horizontal length 539 cm, uniform scale for both x and z. Simulation is performed in the wave frame moving at speed c_{wave}, the speed of the wave as predicted by the TEW code. The resolution is 1024 points in the vertical. (*a*ii–*f*ii) The same as above, for initial magnitude of the perturbation of 0.1 cm^2 s^{-1}.

To further quantify the aforementioned asymmetry in growth, we seed the large solitary-wave solution of amplitude $a/h_1 = 1.51$ with a perturbation in stream function located in front of the wave (at $x_0 = 259$ cm with respect of the peak of the wave)

$$\widetilde{\psi} = \widehat{\psi}\ \mathrm{sech}\left[\chi\ (x - x_0)\right] \cos\left(kx\right)\ \mathrm{sech}\left[\gamma\ \left(z_p - z\right)\right], \tag{4.7}$$

where $\widehat{\psi}$ is the magnitude of the perturbation, k is its wavenumber (we chose $k = 0.5$ cm^{-1} close to the wavenumber of the dominant local instability at the point of maximum displacement) and $\chi = 0.1$ cm^{-1} specifies the horizontal width of the envelope. We perform two tests for $\widehat{\psi} \approx 0.01$ and 0.1 cm^2 s^{-1} respectively.

In order to estimate the amplification factor, we monitor the amplitude of the average density profile. This amplitude of the mean-density isoline displacement is initially $\approx$0.001 cm for the first simulation and 0.01 cm for the second one, respectively. The simulations are performed in a frame of reference moving with the wave, at a spatial resolution of 1024 points in the vertical. (Recall that for this particular resolution, shear instability developing from an unperturbed TEW initial cannot be detected in the density field: see figure 9.) As can be seen from figure 19, roll-ups at the peak of the wave are visible for both simulations, and for the larger perturbation roll-up occurs even in front of the wave's peak amplitude location: see in particular figure 19(*b*ii). The summary of simple model analysis and numerical experiments depicted in figure 18 shows that the simple envelope equation based on

local parallel shear analysis over-predicts the amplification factor of the perturbation. Thus, such simple envelope models result in conservative estimates of the possibility of roll-ups occurring during wave propagation.

4.5. *Stability estimates from strongly nonlinear long-wave models*

Long-wave asymptotics for two-layer fluids can successfully model several features of large nonlinear internal waves (Choi & Camassa 1999; Camassa & Tiron 2011). Next, we use these models to produce direct analytical expressions for the quantities that govern the self-induced shear instability we have examined in the previous section. First, we derive an approximation for the Richardson number along the profile of a solitary wave in a continuous stratification with a thin pycnocline, using the predictions of the strongly nonlinear model (Choi & Camassa 1999) with the choice of parameters appropriately adjusted to include the presence of a finite-width pycnocline (Camassa & Tiron 2011). We assume that the pycnocline thickness d is constant along the wave profile. While this assumption can be relaxed for improved accuracy (Camassa & Tiron 2011), for sufficiently thin pycnoclines of the type used in this study spatial variations in thickness can be neglected at first.

We fix the location $X = x - ct$ along the wave profile, where c denotes the wave phase speed. The Richardson number is defined as

$$Ri(z) = -\frac{\rho'(z)g}{\rho(z)u'(z)^2}. \tag{4.8}$$

The derivative of the horizontal velocity u and of the density ρ can be approximated by $u'(z) \approx \Delta u/d$ and $\rho'(z) \approx -\Delta\rho/d$, respectively, where Δu is the jump in velocity across the interface, $\Delta\rho = \rho_2 - \rho_1$, the difference between the densities of the two layers, and d is the thickness of the pycnocline. We also approximate the density inside the pycnocline by the average value ρ_{av}. We thus have

$$Ri \approx \frac{gd\Delta\rho}{\rho_{av}(\Delta u)^2}. \tag{4.9}$$

By neglecting $O(\epsilon^2)$ correction terms (where $\epsilon = H/L$ is the long wave parameter with H the fluid layer height and L a typical horizontal length scale), the velocity jump at the interface Δu can be written as

$$\Delta u(\zeta) = c\left(\frac{h_1}{\eta_1} - \frac{h_2}{\eta_2}\right), \tag{4.10}$$

where ζ is the interface displacement with respect to the quiescent state, whereas $\eta_1 = h_1 - \zeta$ and $\eta_2 = h_2 + \zeta$ are the widths of the two layers: see Camassa *et al.* (2006).

Thus the Richardson number at any X location of the wave profile can be expressed solely in terms of the interfacial displacement

$$Ri(X) = \frac{g\,d\,\Delta\rho}{\rho_{av}}\left[\frac{(h_1 - \zeta(X))(h_2 + \zeta(X))}{cH\zeta(X)}\right]^2. \tag{4.11}$$

Dropping of higher-order terms in (4.11) is justified, since the variation of pycnocline width along the wave profile has been neglected in this simple estimate, which can induce an error more significant than that of the long-wave asymptotic $O(\epsilon^2)$ terms.

This formula can be further manipulated by substituting the phase speed of the solitary wave in terms of the signed wave amplitude a (Choi & Camassa 1999),

$$\frac{c^2}{c_0^2} = \frac{(h_1 - a)(h_2 + a)}{h_1 h_2 - (c_0^2/g)a}, \tag{4.12}$$

with c_0 the linearized long internal wave speed,

$$c_0^2 = \frac{g\, h_1 h_2\, \Delta\rho}{\rho_1 h_2 + \rho_2 h_1}, \tag{4.13}$$

to read

$$Ri(X) = \frac{d\,(\rho_1 h_2 + \rho_2 h_1 + a\,\Delta\rho)}{\rho_{av} H^2}\,\frac{(\zeta(X) - h_1)(\zeta(X) + h_2)}{(a - h_1)(a + h_2)} \times \left(\frac{h_1}{\zeta(X)} - 1\right)\left(\frac{h_2}{\zeta(X)} + 1\right). \tag{4.14}$$

This equation can be used to evaluate the (X, ζ) location(s) along the wave profile where the Richardson number first becomes critical as functions of the wave amplitude parameter a. Setting $Ri = 1/4$ yields a rational equation for $\zeta(X)$, whose solution, subject to the constraint $a < \zeta(X) < 0$ for waves of depression, can in turn be used to find the possible locations $X = \pm X_c$ where the self-induced shear flow can become critical.

Finally, the minimum Richardson number along the wave profile is located at the maximum displacement of the pycnocline, where the velocity jump is maximum. Setting $X = 0$ in (4.14) (with $\zeta(0) = a$) yields

$$Ri_{min}(a) = \frac{d(\rho_1\, h_2 + \rho_2\, h_1 + a\,\Delta\rho)}{\rho_{av} H^2}\left(\frac{h_1}{a} - 1\right)\left(\frac{h_2}{a} + 1\right). \tag{4.15}$$

Next, model results such as (4.14) and (4.15), together with the parallelized shear analysis of § 4.4, can be assembled into a simple predictive criterion for shear instability manifestations.

4.6. *Amplitude threshold for manifestation of shear instability*

In this final section we explore the stability properties of waves of various amplitudes on the same background stratification as the large-amplitude wave ($a/h_1 = 1.51$) investigated in the previous sections, in an effort to determine a threshold amplitude for the manifestation of instability. We focus on the stability properties at the peak of the wave, where the shear is maximal (and thus, when the flow is locally unstable, the growth rates of the unstable normal modes are maximal). We find that for all the locally unstable waves investigated, the group velocity of the unstable modes at this particular location is negative, suggesting that the flows under consideration can only be *convectively* unstable. Under this assumption, we construct an estimate of the amplification of a perturbation that traverses the region of local instability (4.6) by taking the growth rate at the peak as an upper bound for the growth rate across the region of local instability. The time of travel of the perturbation in the unstable region T_w is approximated by L_{Ri}/c_R, where L_{Ri} is the length of the pocket with $Ri < 1/4$ (which, as shown in the previous section, is an excellent estimate for the extent of the region of local instability), and c_R is the phase speed of the fastest growing mode at the peak of the wave.

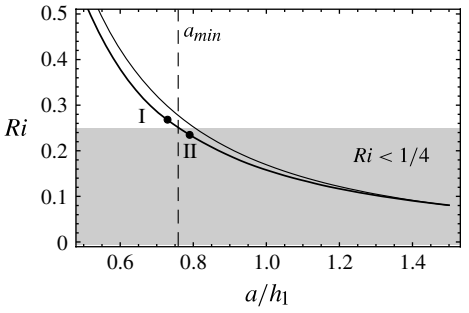

FIGURE 20. The thick line marks the minimum Richardson number at the peak of the wave as a function of the wave amplitude, whereas the thin line corresponds to the prediction using the two-layer approximation. The circles mark waves of amplitudes a/h_1 0.73, 0.79 respectively. The shaded area ($Ri < 1/4$) corresponds to the domain where the necessary condition for local instability is satisfied.

We remark that Troy & Koseff (2005) and Fructus *et al.* (2009) constructed a similar estimate by considering *only half* of the pocket of $Ri < 1/4$, based on the assumption that the shear instability originates at the centre of the wave. In fact, as can be seen in figure 19, for sufficiently large magnitudes of the initial perturbation roll-ups can develop *before* the peak of the wave. While our numerical experiments reveal that the local growth rates are inhibited in the front of the wave, this is expected to be a first-order (in the long wave parameter) correction. Thus we argue that considering the full extent of the area of local instability offers a more robust estimate for the amplification factor.

In order to isolate an amplitude range for which we expect to identify local instability within the flow field, we first evaluate the minimum Richardson number at the peak of the wave as a function of the wave amplitude. We thus identify a minimal amplitude $a_{min}/h_1 \approx 0.76$ corresponding to $Ri_{min} = 1/4$: see figure 20, which also shows that the two-layer approximation (appropriately adjusted to include the presence of a finite-width pycnocline as in Camassa & Tiron 2011) furnishes a reasonable estimate for this minimum Richardson number (see relation (4.15), § 4.5). Furthermore, by evaluating the local spectrum at the point of maximum displacement for two waves bracketing the threshold amplitude a_{min} (corresponding to the points I and II in figure 20), we confirm again that the $Ri < 1/4$ is an accurate indicator of local instability. Indeed, we have identified unstable normal modes only for the amplitude II: 0.79.

Next, we evaluate the unstable local spectrum in the amplitude range a_{min} to maximal: see figure 21, where we depict the maximum growth rate and the phase speed corresponding to the dominant growing mode, both corresponding to the peak of the wave.

Finally we determine the length of the area with $Ri < 1/4$: see figure 22, showing this area for several of the waves investigated, and figure 23, where we show the dependence of the length of these areas on the amplitudes. As can be observed from both of these figures, the two-layer model offers reasonable estimates for the location of the points that limit the horizontal extent of this area (this location can be determined by setting $Ri = 1/4$ in relation (4.14)). (We remark that the height associated with these points has a weak dependence on amplitude, suggesting a critical

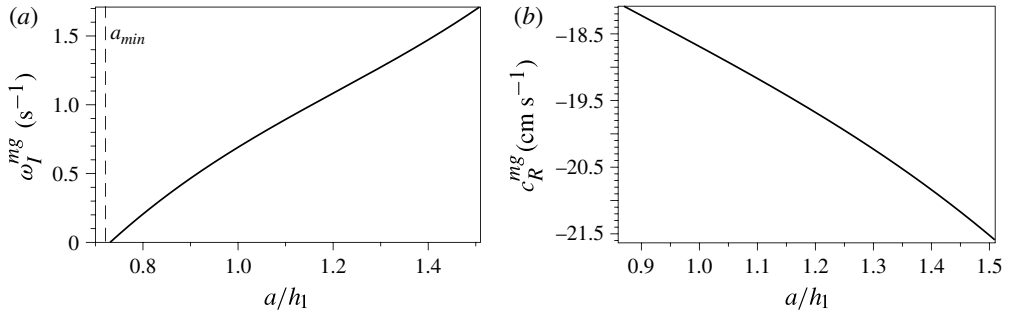

FIGURE 21. (*a*) Maximum growth rate at the peak as a function of amplitude. The dashed vertical line marks the amplitude $a_{min}/h_1 \approx 0.76$, corresponding to the wave that has the minimum Richardson number at the peak of the wave $Ri_{min} = 1/4$. (*b*) Phase speed of the dominant unstable mode at the peak as a function of amplitude.

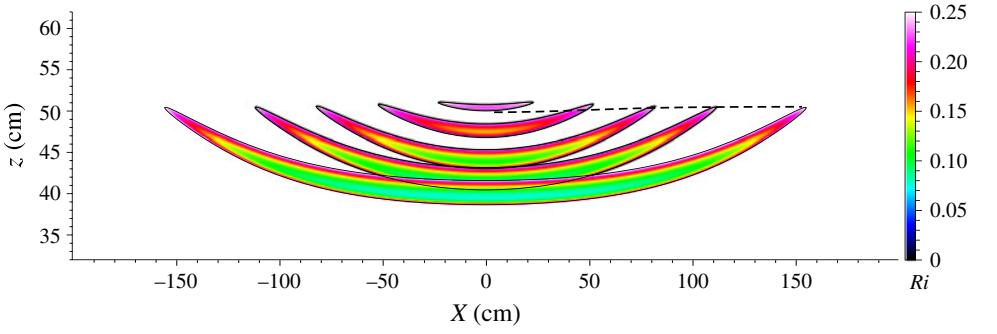

FIGURE 22. (Colour online) Regions with Richardson number smaller than 1/4 for waves of amplitudes a/h_1 0.79, 0.98, 1.14, 1.23 and 1.51 respectively. The dashed line marks the two-layer model estimate for the horizontal extent of this area: see relation (4.14).

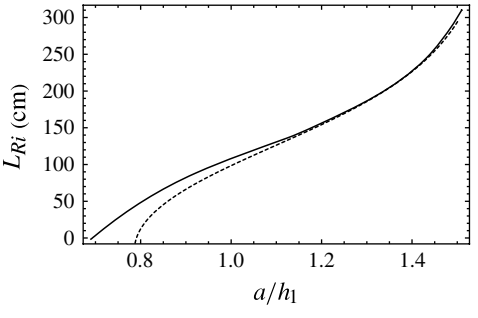

FIGURE 23. Dependence of the length of the area of local instability on the wave amplitude. The dashed line marks the the two-layer model estimate.

height mechanism that could be obtained by scaling arguments independent of the details of a model.)

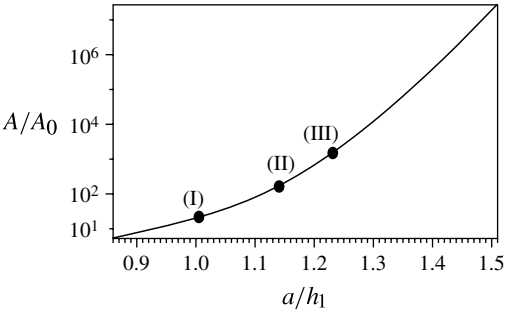

FIGURE 24. Amplification factor (defined by relation (4.6)) as a function of wave amplitude.

Having determined the extent of the area of local instability and the growth rate and phase speed of the dominant unstable mode at the peak of the waves, we can estimate the amplification factor, which we depict in figure 24. For waves of amplitude $a_{min}/h_1 < a/h_1 < 0.9$ the amplification factor is less than 10, thus we do not expect Kelvin–Helmholtz billows to develop for this amplitude range, even for relatively large magnitudes of the initial perturbation. Note that this particular value for the amplification factor does not represent a rigorous threshold for instability, but rather provides an indication as to whether the shear instability would eventually become visible in the density field. Another factor that might inhibit shear instability development is when the length of the area of instability becomes comparable to the the dominant instability wavelength (which is $\approx$12 cm based on the local linear stability analysis). Note, however, that in our case this happens when $a/h_1 < 0.7$, an amplitude range already excluded by the criterion based on the amplification factor. To demonstrate the effectiveness of the threshold for the manifestation of shear instability identified above, we have performed numerical simulations for the evolution of several waves with amplitudes marked in figure 24 (a/h_1 of 1.023, 1.14 and 1.23 respectively: see figures 25–27). In all instances, we use an initial perturbation stream function of magnitude 0.001 cm^2 s^{-1} and with wavenumber $k = 0.5$ cm^{-1} (close to the dominant instability wavenumber),

$$\psi(x, z, 0) = \widehat{\psi}_0 \ \mathrm{sech}^2 \left[\kappa(z_p - z)\right] \cos kx, \tag{4.16}$$

where z_p is the centre of the pycnocline at the maximum displacement, the parameter $\kappa = 0.2$ cm^{-1} is chosen so that the thickness of the perturbation-band is $\approx$10 cm, and $\widehat{\psi}_0$ is the magnitude of the perturbation.

We remark that a wave of amplitude $a/h_1 = 1.23$ emerging from a step initial condition as in the experiment does not exhibit shear instability during its evolution, as seen in both experimental and numerical (Tiron 2009, §4.2) investigations. However, as shown in figure 27, we can detect shear instability when a sufficiently large perturbation is superimposed on a travelling-wave solution of this amplitude.

5. Discussion

We have carried out a numerical and analytical study of the stability of solitary waves of large amplitude in a near two-layer stratification, working for definiteness with parameters from the laboratory experiments reported in Grue *et al.* (1999). While we have worked with dimensional quantities and 'hardware' parameters chosen from an actual experimental set-up, many of the results we present reflect general behaviour

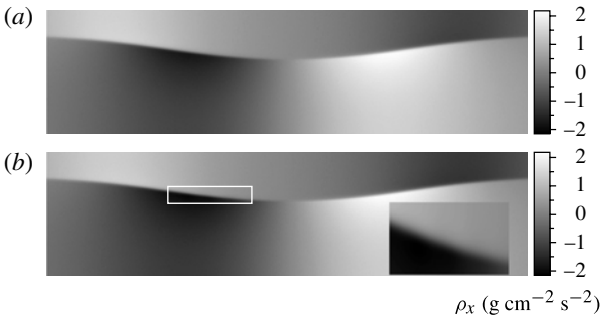

FIGURE 25. Snapshots of the horizontal pressure gradient from the time evolution simulation of a wave of amplitude $a/h_1 = 1.023$, perturbed with a monochromatic perturbation (4.16) of non-dimensional amplitude 10^{-3} at (*a*) $t = 0$ s and (*b*) $t = 5$ s. Only a section of the computational domain (period $L = 1232$ cm) is shown, centred at the peak of the wave, of horizontal length 300 cm, uniform scale for both x and z. (The simulation is performed in the wave frame moving at the speed c_{wave}, the speed of the wave as predicted by the TEW code.) Resolution is 512 points in the vertical.

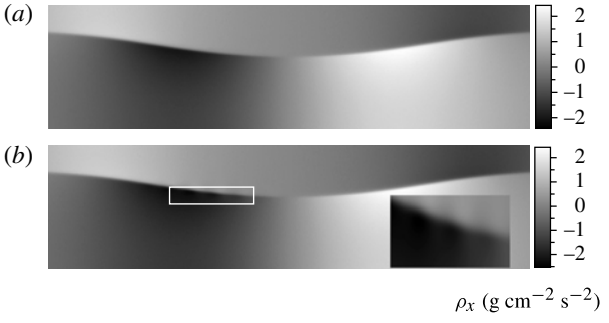

FIGURE 26. The same as figure 25, $a/h_1 = 1.14$.

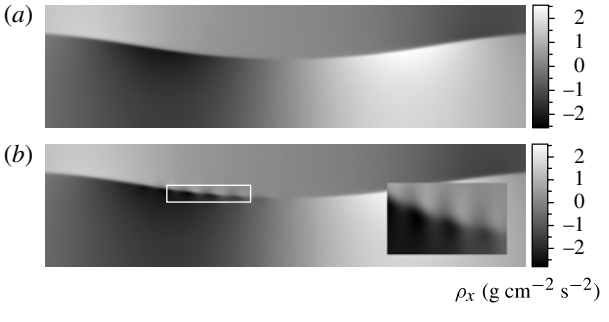

FIGURE 27. The same as figure 25, $a/h_1 = 1.23$.

of internal waves with relatively thin pycnoclines, as we have checked by varying these parameters for several different cases.

In order to identify the origin of shear instability for waves of large amplitude, we have studied the propagation of solitary-wave solutions of Euler equations (obtained with a variant of the algorithm presented in Turkington *et al.* 1991, which we describe in § 2 and appendix A). Our resolution study has demonstrated the convergence of both the evolution code and of the initial condition. While demonstrating convergence, we have also provided evidence on the stability properties of the flow: sufficiently large numerical errors in the initial data induce a first episode of shear instability which can lead to development of Kelvin–Helmholtz billows. These, however, are advected away from the region of maximum displacement of the pycnocline, leaving the wave in a state of equilibrium. Thus, no global self-sustained instability of the whole wave has emerged from our study.

To analyse this further, we have performed a local spectral stability analysis of the steady solution. The stability analysis reveals that sufficiently large waves develop locally unstable shear flows in a finite region around the point of maximum displacement whose horizontal extent is very well approximated by the $Ri < 1/4$ criterion. The phase speed and the group velocity associated with the unstable local modes are negative in the frame of reference of the wave, suggesting that the flow is convectively unstable, and thus precluding the existence of a global self-sustained mode. Furthermore, the wavenumber associated with the maximal growth rates of eigenmodes was found to be almost constant across the region of local instability, and consistent with the wavenumbers observed in numerical simulations. The finite extent of the region of shear instability, combined with the information of phase and group velocity from the real part of unstable eigenvalues, gives an estimate of the time duration available for perturbation growth. This information can be estimated analytically by the strongly nonlinear two-layer models, which can accurately predict the minimum Richardson number along the wave profile and therefore the horizontal and vertical extent of the area of local instability. Furthermore, two-layer models can be extended (Camassa & Tiron 2011) to afford a reasonable reconstruction of both the density and velocity profiles of solitary waves in near two-layer stratifications even when the transition layer has relatively large thickness. Explicit closed-form solutions are available for these models and could be exploited for estimating the local spectrum of solitary waves. We have also refined a simple amplitude equation for the growth of a monochromatic perturbation (associated with the optimally growing normal modes) across the region of local instability. Combined with the analytical results from asymptotic models of long wave propagation, this approach can provide a rough predictive estimate for the possibility of Kelvin–Helmholtz roll-ups during the evolution of a given amplitude internal solitary wave. This analysis merits further investigation and extensions, as it would allow exploring *a priori* the stability properties of solitary waves for a large class of stratifications relevant to geophysical applications.

The class of solitary waves we study appears to be mathematically stable in the Lyapunov sense. We note that an analytical treatment of this problem, as part of the general topic of stability of stratified flows, seems to present some formidable difficulties (as discussed, among others, by Benjamin 1986), which in fact have led to incorrect results published in the literature (see e.g. Friedlander 2001 for a critique of past work on this particular topic) even for the presumably simpler case of parallel stratified shear flow solutions. While we do not attempt a rigorous mathematical proof for the stability conjecture, to the best of our knowledge our study is the first to provide a careful numerical assessment of the question of global stability of solitary internal waves, which we have corroborated with numerous checks and validations on

both the travelling-wave solution and the time-evolution code (presented in §§ 2.1, 4.1 and appendix B), based on analytical tools whenever available. It is interesting to note in this context the analysis by Kataoka (2006), which claims that solitary-wave solutions in two-layer fluids are absolutely stable except for extremely low densities of the lighter layer, a situation which essentially corresponds to the surface gravity waves case. Kataoka's (2006) result in fact provides an extreme example of internal waves being stable as a whole, even though the shear is unstable locally, in fact ill-posed due to the velocity jump across the interface between the layers in an inviscid set-up.

In order to provide the evidence to support our stability conjecture, we have refined the TEW algorithm to determine highly accurate travelling-wave solutions that would also remain steady solutions for the time-dependent code. As shown by comparison with the results of Carr *et al.* (2011), control of numerical perturbations requires high accuracy, without which nonlinear saturation of instabilities can develop in simulations of large-amplitude solitary-wave propagation.

It is also important to draw a distinction between our approach and the *forced* problem, performed in the wave reference frame, in which upstream boundary conditions are assigned (reflecting an assumed constant speed of the wave which is stationary in the computational domain), which is the set-up of Lamb & Farmer (2011). The ensuing study is naturally that of a 'signalling problem', in which a time-dependent perturbation is applied at the upstream boundary and varies spatially downstream. While clearly interesting, this problem is quite different from the spatially doubly infinite or periodic set-up, as pointed out in § 4.3. Nonetheless, it is worth noting that the weak nature of the shear instability observed in both numerical simulations and laboratory experiments leads to a minimal energy depletion of the solitary travelling wave in response to perturbations (when compared to the energy of the base flow), which implies minimal upstream fluid velocity variations once in the frame of reference of the wave (see for instance Camassa & Viotti 2012 for a discussion of these points). This of course makes the signalling problem practically relevant, while providing evidence in a different form of the inherent stability of solitary waves in this configuration.

Our study has also brought forth some shortcomings of simple models of shear instability amplification. In particular, the marked front–back asymmetry in growth observed in our numerical simulations (and laboratory experiments such as Grue *et al.* 1999 and Fructus *et al.* 2009) requires a more in-depth approach. Growth rates appear to be inhibited in front of the wave's maximum, while, conversely, they seem to be enhanced downstream from that location. As pointed out in Camassa & Viotti (2012), non-normality of the Taylor–Goldstein spectrum can lead to decay of perturbations in regions upstream of an internal wave maximum, so offering a possible mechanism for growth inhibition. Further, some of these effects may be predicted by an extension to the next order of the asymptotic expansion in the long wave parameter, although this is proving to be a rather involved calculation. Ultimately, this would help us understand the detailed physical mechanisms responsible for unstable growth, and how this relates to the spatial variation of the flow dictated by the solitary internal wave propagation.

Acknowledgements

The authors wish to thank A. Sallerson for her assistance with preliminary work on the TEW and VARDEN numerical codes, D. Adalsteinsson for help with his data-analysis and visualization software DataTank, and W. Choi for many valuable discussions. Most of the intensive numerics was performed on the 'Topsail' cluster (an

outgrowth of an initial seed supported by an NSF MRI-0116625 grant), managed by UNC-ITS Research Computing staff, whose assistance is gratefully acknowledged. This research is supported by NSF grants DMS-0509423, CMG-0620687, DMS-1009750, and RTG DMS-0943851. R.T. acknowledges partial support by the Korea Advanced Institute of Science and Technology (KAIST) while this work was being completed for publication.

Appendix A. The TEW algorithm

In this appendix we summarize the computational method for determining fully nonlinear solitary-wave solutions of Euler equations in continuous stratification presented in Turkington *et al.* (1991) (the TEW algorithm).

A.1. *Variational principle*

Equation (2.1) admits a variational formulation. Let the objective and constraint functionals, respectively, be defined as

$$E(\eta) = \int_D \frac{1}{2} |\nabla \eta|^2 \, \overline{\rho}(z - \eta) \, \mathrm{d}x \, \mathrm{d}z, \tag{A 1}$$

and

$$F(\eta) = \int_D f(z, \eta) \, \mathrm{d}x \, \mathrm{d}z, \tag{A 2}$$

with

$$f(z, \eta) = \frac{1}{H} \int_0^{\eta} [\overline{\rho}(z - \eta) - \overline{\rho}(z - \xi)] \, \mathrm{d}\xi. \tag{A 3}$$

Then a pair (η, λ) that satisfies the condition

$$E(\eta) \to \min \quad \text{subject to } F(\eta) = A > 0 \tag{A 4}$$

is a solution of (2.1). It is straightforward to verify that if η is a minimizer and λ is the associated Lagrange multiplier then (2.1) holds, since

$$E'(\eta) = \mathrm{M}\eta, \quad F'(\eta) = -\frac{\eta}{H} \overline{\rho}'(z - \eta), \tag{A 5}$$

where prime denotes the functional derivative in η. Note that $c^2 E$ represents the kinetic energy of the wave in the laboratory frame whereas $g\,HF$ represents the potential energy of the wave disturbance. Thus the physical interpretation of the variational principle mentioned above is quite appealing: a solitary-wave solution minimizes the kinetic energy of the admissible variations for a prescribed potential energy.

A.2. *Semilinear form of the eigenvalue problem*

An extra step in the numerical solution of (2.1) introduced by Turkington *et al.* (1991) consists in a change of variable replacing η in favour of a new unknown:

$$\phi = s(z) - s(z - \eta) \quad \text{with } s(z) = \int_0^z \sqrt{\overline{\rho}(\xi)} \, \mathrm{d}\xi. \tag{A 6}$$

With this new variable, the *quasi-linear* eigenvalue problem (2.1) in $\eta = z - s^{-1}(s(z) - \phi)$ is transformed into a *semilinear* eigenvalue problem in ϕ,

$$-\Delta\phi + s''(z) - s''(s^{-1}(s(z) - \phi)) = -\frac{2\lambda}{H}[z - s^{-1}(s(z) - \phi)]s''(s^{-1}(s(z) - \phi)), \quad (A\,7)$$

with boundary conditions

$$\phi = 0 \quad \text{on } \partial D, \quad \phi \to 0 \quad \text{as } x \to \pm\infty. \quad (A\,8)$$

The objective and constraint functionals (A 1), (A 2) become

$$E(\phi) = \int_D \left[\frac{1}{2}|\nabla\phi|^2 + e(z, \phi)\right] \mathrm{d}x\,\mathrm{d}z, \quad (A\,9)$$

and

$$F(\phi) = \int_D f(z, \phi)\,\mathrm{d}x\,\mathrm{d}z, \quad (A\,10)$$

where

$$e(z, \phi) = \int_0^\phi [s''(z) - s''(s^{-1}(s(z) - \xi))]\,\mathrm{d}\xi, \quad (A\,11)$$

and

$$f(z, \phi) = -\frac{2}{H}\int_0^\phi [z - s^{-1}(s(z) - \xi)]s''(s^{-1}(s(z) - \xi))\,\mathrm{d}\xi. \quad (A\,12)$$

The semilinear eigenvalue problem (A 7) can be compactly rewritten in terms of the functional derivatives of f and e with respect to ϕ (denoted by ϕ-subscripts) as

$$-\Delta\phi + e_\phi(z, \phi) - \lambda f_\phi(z, \phi) = 0. \quad (A\,13)$$

Finally, at the basis of the minimization technique lies the assumption that the objective functional E is convex, which Turkington *et al.* (1991) show can be enforced by requiring

$$\max [e_{\phi\phi}]_- < (\pi/H)^2\,. \quad (A\,14)$$

(One defines, for any scalar function χ, $\max[\chi]_- \equiv \max_{\chi<0}|\chi|$ and $\max[\chi]_+ \equiv \max_{\chi>0}|\chi|$.)

It is important to notice that the above condition is sufficient but not necessary for convexity, and that it is not met for many stratifications with narrow pycnoclines, such as the ones we focus on in our work.

A.3. *Iterative scheme*

Turkington *et al.* (1991) introduced a globally convergent iterative algorithm that solves the semilinear problem (A 7) by casting it in the form of a quadratic programming subproblem. In the following, we outline their strategy, emphasizing the steps which are relevant to our numerical implementation. The convergence of the iterative scheme relies upon the convexity of the two functionals $F + \beta E$ and E, respectively, where the constant β is chosen such that

$$\beta(\pi^2/H^2 - q) - r > 0, \quad (A\,15)$$

with q, r denoting the bounds

$$q = \max\,[e_{\phi\phi}(z,\phi)]_-, \quad r = \max\,[f_{\phi\phi}(z,\phi)]_-\,. \tag{A 16}$$

Then, by choosing

$$\alpha = \max\,[e_{\phi\phi}(z,\phi)]_+, \tag{A 17}$$

E can be split as

$$E = E_+ - E_-, \tag{A 18}$$

with

$$E_+ = \int_D \left[\frac{1}{2}\,|\nabla\phi|^2 + \frac{\alpha}{2}\phi^2\right]\,\mathrm{d}x\,\mathrm{d}z, \tag{A 19}$$

convex and quadratic, and

$$E_- = \int_D \left[\frac{\alpha}{2}\phi^2 - e(z,\phi)\right]\,\mathrm{d}x\,\mathrm{d}z, \tag{A 20}$$

convex.

Thus, with the above notation, the iterative algorithm can be described as follows. Let ϕ^0 be an initial condition satisfying $F(\phi^0) = A$. The iterative step $\phi^k \to \phi^{k+1}$ consists in solving the problem

$$\begin{aligned} &E_+(\phi) - E_-(\phi^k) - \langle E'_-(\phi^k), \phi - \phi^k\rangle \\ &\quad \to \min \text{ over } F(\phi^k) + \langle F'(\phi^k) + \beta E'(\phi^k), \phi - \phi^k\rangle \geqslant A, \end{aligned} \tag{A 21}$$

where $\langle\cdot\,,\cdot\rangle$ denotes the inner product

$$\langle u, v\rangle = \int_D u\,v\,\mathrm{d}x\,\mathrm{d}z. \tag{A 22}$$

Appendix B. Validation of the time-dependent code: linear growth of the shear instability

Almgren *et al.* (1998) validated the evolution code by replicating numerically the mixing layer experiments reported in Brown & Roshko (1974) and comparing against their experimental data. However, since experiments introduce uncertainties, in particular for inherently unstable flows such as mixing layers, a more stringent test of code validity is given by the exact solutions of the underlying model equations. In this work, we present two such tests: the first consists of the time evolution within the class of solitary-wave solutions of Euler equations (see § 3) while the second is given by the initial linear stage of growth of shear instabilities, which we test in this appendix.

We simulate the time evolution of a parallel shear constructed with the density stratification and the shear from the maximum displacement of the pycnocline for the wave with amplitude $a/h_1 = 1.51$, perturbed with a normal mode solution of the Taylor–Goldstein equation (4.1) with wavenumber $k = 77\pi/5 \approx 0.4$ cm^{-1} close to the wavenumber of the dominant instability. The initial magnitude of the perturbation in stream function is 0.001 cm^2 s^{-1} and the corresponding amplitude of the isolines of density is $\approx 10^{-4}$cm (since the displacement $\sim\psi/(u_0 - c)$). The computational domain consists of a square 77 cm × 77 cm with slip boundary conditions at top and bottom

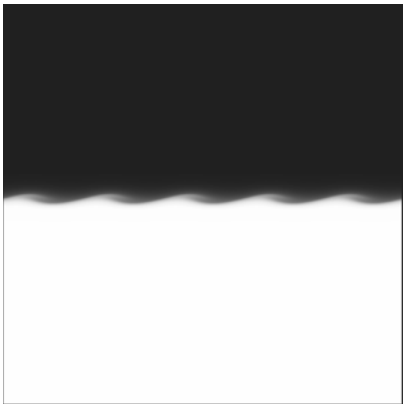

FIGURE 28. Snapshot of the density field at time $t = 5$ s from the time-evolution simulation of a parallel shear constructed with the density and horizontal velocity profile from the maximum displacement of the wave of amplitude $a/h_1 = 1.51$, perturbed with an unstable normal mode of wavenumber $k = 77\pi/5 \approx 0.4\,\mathrm{cm}^{-1}$. The computational domain is of 77 cm × 77 cm, periodic boundary conditions in the horizontal direction, while the resolution is of 1024 points in the vertical.

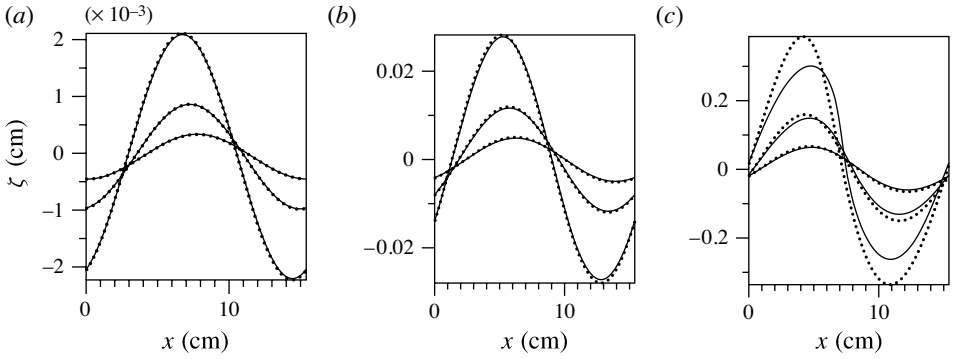

FIGURE 29. Density isolines corresponding to the average density at (*a*) 0.5, 1, 1.5 s; (*b*) 2, 2.5, 3 s; (*c*) 3.5, 4, 4.5 s. Solid line, linear theory; dotted line, numerical simulation with VARDEN.

and periodic boundary conditions in the horizontal direction. The spatial discretization is 1024 points in the vertical. We perform the simulation in the laboratory frame where the phase speed of growing normal modes (and hence the horizontal excursion of the the density isolines in the initial stage of linear growth) is relatively small ($\approx$1 cm s^{-1}).

We first construct the perturbation density field associated with the normal mode $\widetilde{\rho} = -\rho_0'(z)/(u_0 - c)\psi$, where ψ is the perturbation stream function and $c \approx (-1.02762 + 4.12321\,\mathrm{i})\ \mathrm{cm\,s}^{-1}$ is the complex eigenvalue velocity. We can thus monitor the behaviour of the average density isoline predicted by the linear theory. As can be seen in figure 29, the linear theory compares very well with the direct numerical simulation, up to $t \approx 4.5$ s when the magnitude of the isoline displacement $\psi/(u_0 - c)$ becomes large and so the approximation for the density perturbation is

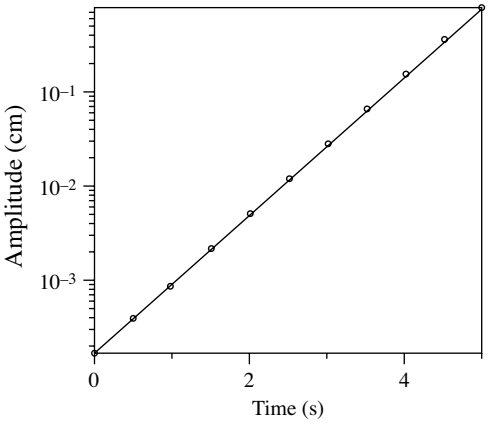

FIGURE 30. Amplitude (half of the distance trough to crest corresponding to the average density isoline). Solid line, linear theory $A(t=0)\,\mathrm{Exp}(k\,c_I\,t)$; circles, numerical simulation with VARDEN.

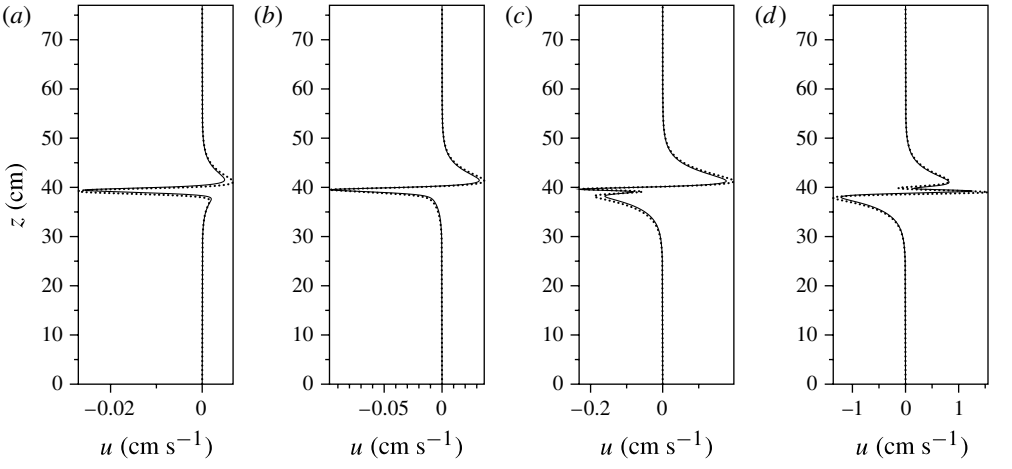

FIGURE 31. Perturbation horizontal velocity profile measured at $x = 8$ cm from the left boundary of the domain at times (*a*) 2 s, (*b*) 3 s, (*c*) 4 s, (*d*) 5 s. Solid line, linear theory; dotted line, numerical simulation with VARDEN.

no longer accurate. Nonetheless, the growth rate of the amplitude from the direct numerical simulation (measured as distance crest-to-trough along the isoline) matches remarkably well with the estimate based on the linear theory, for the entire time range of the simulation $t \in (0, 5\ \mathrm{s})$: see figure 30. We also display in figure 31 the horizontal velocity profile measured at a fixed location $x = 8$ cm from the left boundary of the domain. Notice again the excellent agreement with the linear theory prediction even at $t = 5$ s, when the behaviour of instability becomes nonlinear, as evidenced in figure 28.

REFERENCES

ALMGREN, A. S., BELL, J. B., COLELLA, P., HOWELL, L. H. & WELCOME, M. L. 1998 A conservative adaptive projection method for the variable density incompressible Navier–Stokes equations. *J. Comput. Phys.* **142**, 1–46.

ARNOLD, V. I. 1992 *Ordinary Differential Equations*. Springer.

BARAD, M. F. & FRINGER, O. B. 2010 Simulations of shear instabilities in interfacial gravity waves. *J. Fluid Mech.* **644**, 61–95.

BENJAMIN, T. B. 1966 Internal waves of finite amplitude and permanent form. *J. Fluid Mech.* **25**, 241–270.

BENJAMIN, T. B. 1972 The stability of solitary waves. *Proc. R. Soc.* A **328**, 153–182.

BENJAMIN, T. B. 1986 On the Boussinesq model for two-dimensional wave motions in heterogeneous fluids. *J. Fluid Mech.* **165**, 445–474.

BONA, J. 1975 On the stability theory of solitary waves. *Proc. R. Soc. Ser.* A **344**, 363–374.

BRIGGS, R. J. 1964 *Electron-stream Interaction with Plasmas*. MIT Press.

BROWN, G. L. & ROSHKO, A. 1974 On density effects and large structure in turbulent mixing layers. *J. Fluid Mech.* **64**, 775–816.

CAMASSA, R., CHOI, W., MICHALLET, H., RUSÅS, P.-O. & SVEEN, J. K. 2006 On the realm of validity of strongly nonlinear asymptotic approximations for internal waves. *J. Fluid Mech.* **549**, 1–23.

CAMASSA, R. & TIRON, R. 2011 Optimal two-layer approximation for continuous density stratification. *J. Fluid Mech.* **669**, 32–54.

CAMASSA, R. & VIOTTI, C. 2012 On the response to upstream disturbances of large-amplitude internal waves. *J. Fluid Mech.* **702**, 59–88.

CARR, M., KING, S. E. & DRITSCHEL, D. G. 2011 Numerical simulation of shear-induced instabilities in internal solitary waves. *J. Fluid Mech.* **683**, 263–288.

CHOI, W. & CAMASSA, R. 1999 Fully nonlinear internal waves in a two-fluid system. *J. Fluid Mech.* **396**, 1–36.

DUDA, T. F., LYNCH, J. F., IRISH, J. D., BEARDSLEY, R. C., RAMP, S. R., CHIU, C.-S., TANG, T. Y. & YANG, Y. J. 2004 Internal tide and nonlinear internal wave behaviour at the continental slope in the northern South China Sea. *IEEE J. Ocean. Engng* **29**, 1105–1130.

FRIEDLANDER, S. 2001 On nonlinear instability and stability for stratified shear flow. *J. Math. Fluid Mech.* **3**, 82–97.

FRUCTUS, D., CARR, M., GRUE, J., JENSEN, A. & DAVIES, P. 2009 Shear-induced breaking of large internal solitary waves. *J. Fluid Mech.* **620**, 1–29.

GRUE, J., JENSEN, A., RUSÅS, P.-O. & SVEEN, J. K. 1999 Properties of large-amplitude internal waves. *J. Fluid Mech.* **380**, 257–278.

HAZEL, P. 1972 Numerical studies of the stability of stratified shear flows. *Annu. Rev. Fluid Mech.* **38**, 395–425.

HELFRICH, K. R. & MELVILLE, W. K. 2006 Long nonlinear internal waves. *Annu. Rev. Fluid Mech.* **38**, 395–425.

HOLYER, J. Y. 1979 Large amplitude progressive interfacial waves. *J. Fluid Mech.* **93**, 433–448.

HOWARD, L. N 1961 Note on a paper of John W. Miles. *J. Fluid Mech.* **10**, 509–512.

HUERRE, P. 2007 Open shear flow instabilities. In *Perspectives in Fluid Dynamics: A Collective Introduction to Current Research*, sixth edition, pp. 159–229. Cambridge University Press.

HUERRE, P. & MONKEWITZ, P. 1985 Absolute and convective instabilities in free shear layers. *J. Fluid Mech.* **159**, 151–168.

HUERRE, P. & MONKEWITZ, P. 1990 Local and global instabilities in spatially developing flows. *Annu. Rev. Fluid Mech.* **22**, 473–537.

KATAOKA, T. 2006 The stability of finite-amplitude interfacial solitary waves. *Fluid Dyn. Res.* **38**, 831–867.

LAMB, K. G. 2002 A numerical investigation of solitary internal waves with trapped cores formed via shoaling. *J. Fluid Mech.* **451**, 109–144.

LAMB, K. G. & FARMER, D. 2011 Instabilities in an internal solitary-like wave in the Oregon Shelf. *J. Phys. Oceanogr.* **41**, 67–87.

LONG, R. 1965 On the Boussinesq approximation and its role in the theory of internal waves. *Tellus* **15**, 46–52.

MASLOWE, S. A. & THOMPSON, J. M. 1971 Stability of a stratified free shear layer. *Phys. Fluids* **14**, 453–458.

MILES, J. W. 1963 On the stability of heterogeneous shear flows (part 2). *J. Fluid Mech.* **16**, 209–227.

MOUM, J. N., FARMER, D. M., SMYTH, W. D., ARMI, L. & VAGLE, L. 2003 Structure and generation of turbulence at interfaces strained by internal solitary waves propagating shoreward over the continental shelf. *J. Phys. Oceanogr.* **33**, 2093–2112.

PUCKETT, E. G., ALMGREN, A. S., BELL, J. B., MARCUS, D. L. & RIDER, W. G. 1997 A higher-order projection method for tracking fluid interfaces in variable density incompressible flows. *J. Comput. Phys.* **130**, 269–282.

TIRON, R. 2009 Strongly nonlinear internal waves in near two-layer stratifications: generation, propagation and self-induced shear instabilities. PhD thesis, Mathematics Department, University of North Carolina at Chapel Hill.

TROY, D. & KOSEFF, J. R. 2005 The instability and breaking of long internal waves. *J. Fluid Mech.* **543**, 107–136.

TURKINGTON, B., EYDELAND, A. & WANG, S. 1991 A computational method for solitary internal waves in a continuously stratified fluid. *Stud. Appl. Math.* **85**, 93–127.

YIH, C. 1980 *Stratified Flows*. Academic.